Progress in Solid State Chemistry 68 (2022) 100379

Contents lists available at ScienceDirect

Progress in Solid State Chemistry

journal homepage: www.elsevier.com/locate/pssc

Structure and functional properties of oxides in the $BaO–Al_2O_3$ system: Phosphors, pigments and catalysts

Zhiwei Wang [a], Yuqian Wang [a,b], M.A. Subramanian [c], Peng Jiang [a,*]

[a] Department of Inorganic Nonmetallic Materials, School of Materials Science and Engineering, University of Science and Technology Beijing, Beijing, 100083, China
[b] Beijing National Laboratory for Condensed Matter Physics, Institute of Physics, Chinese Academy of Sciences, Beijing, 100190, China
[c] Department of Chemistry, Oregon State University, Corvallis, OR, 97330, USA

ARTICLE INFO

Keywords:
$BaO–Al_2O_3$ system
Photoluminescent properties
Visible color
Catalytic properties

ABSTRACT

Oxides such as $BaAl_{12}O_{19}$ and $BaAl_2O_4$ in the $BaO–Al_2O_3$ system demonstrate potential for optical applications due to the abundant tetrahedral and octahedral sites in their structures, as well as their high thermal stability, good chemical stability, high surface area and strong light absorption capacity. Rare earth element doping or transition metal ion doping in oxides in the $BaO–Al_2O_3$ system contributes to promising photoluminescent, visible color and catalytic properties. In this review, the structures of $BaAl_{12}O_{19}$, $BaAl_2O_4$, $Ba_3Al_2O_6$, $Ba_4Al_2O_7$, and $Ba_7Al_2O_{10}$ in the $BaO–Al_2O_3$ system are introduced. Their applications in phosphors, pigments and catalysts are also summarized herein.

1. Introduction

Due to their high thermal stability, good chemical stability, facile synthesis and low toxicity, oxides in $BaO–Al_2O_3$ systems, such as $BaAl_{12}O_{19}$ and $BaAl_2O_4$, have been extensively studied for optical applications by introducing rare earth ions or transition metal ions in the last few decades. Their applications are extended to phosphors, pigments, photocatalysts and so on.

Phosphor materials play a very important role in human life as their application fields extend to solid-state lighting, display imaging, emergency instructions, luminescent ceramic glaze, optical thermometry and so on. They are used as solid-state lasers, light emitting diodes (LEDs), plasma display panels (PDPs) or sensors [1].

In the early years, $BaAl_{12}O_{19}:Mn^{2+}$ phosphor with a hexaaluminate structure was an important green-emitting phosphor in plasma display panels (PDPs) and fluorescent lamps (FL). In recent years, phosphor-converted white light-emitting diode (pc-WLED) lighting, which has gradually replaced fluorescent lamps, has been widely integrated into our daily lives due to its high energy efficiency, low energy consumption, reliability, durability, long lifetime, and eco-friendly features [2]. They are also used as backlighting instead of usual fluorescent tubes in LCD televisions. Therefore, there is an increasing amount of research on suitable phosphors for WLEDs. $BaAl_{12}O_{19}:Eu^{2+}$, $BaAl_2O_4:Ce^{3+}$ blue-emitting phosphors and $BaAl_2O_4:Eu^{3+}$ red-emitting phosphor are promising phosphor for WLEDs lighting sources.

$BaAl_{12}O_{19}$ also demonstrates great potential in dual-mode optical thermometry, which is an emerging application of luminescent materials. The fluorescence intensity ratio (FIR) or the fluorescence decay time could be applied in monitoring the temperature. By doping two phosphorous ions in one material, the dual-mode optical thermometry will be sensitive to both parameters at the same time, which greatly improves the flexibility and applicability of fluorescence thermometry.

In addition, an increasing number of studies have also focused on rare-earth-doped alkaline-earth aluminates with long afterglows (persistent luminescence), which can be applied in emergency signalization, microdefect sensing, optoelectronics for image storage, and detectors of high-energy radiation [3]. By codoping Eu^{2+}, R^{3+} (R^{3+} is a rare earth element) in $BaAl_2O_4$, persistent luminescence is observed as R^{3+} increases the number of traps.

In addition to applications in phosphors, recent studies reveal that oxides in the $BaO–Al_2O_3$ system demonstrate promising optical properties in the visible region when doped with higher transition metal concentrations. $BaAl_{12}O_{19}$ and $BaAl_2O_4$ are widely used in high-temperature catalysis because of their high thermal stability and high surface area.

Due to the valuable applications in optical properties, the structures and optical applications of oxides in the $BaO–Al_2O_3$ system are summarized and presented.

* Corresponding author.
E-mail address: jiangp@ustb.edu.cn (P. Jiang).

https://doi.org/10.1016/j.progsolidstchem.2022.100379

Available online 28 October 2022

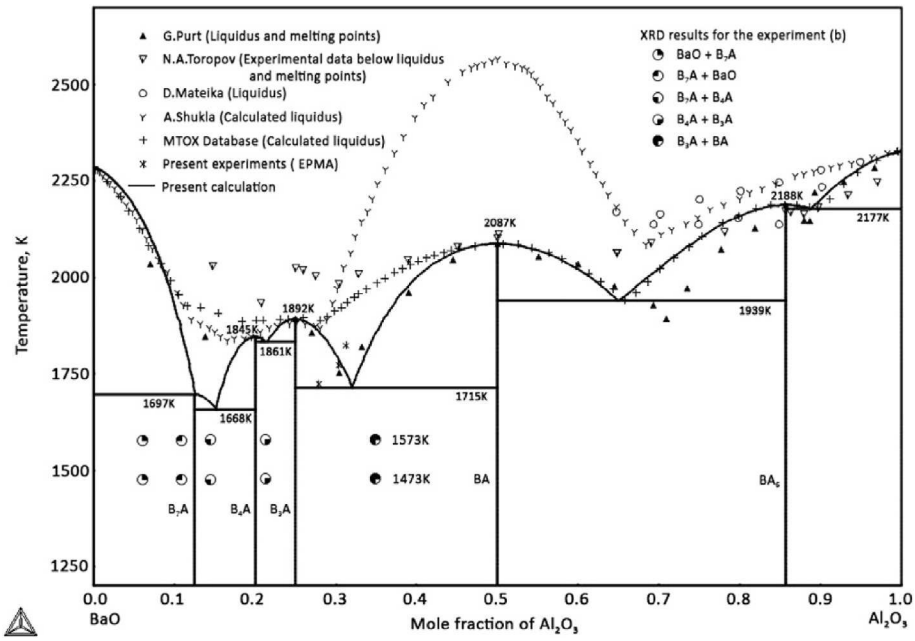

Fig. 1. The phase diagram of the BaO–Al_2O_3 system [5].

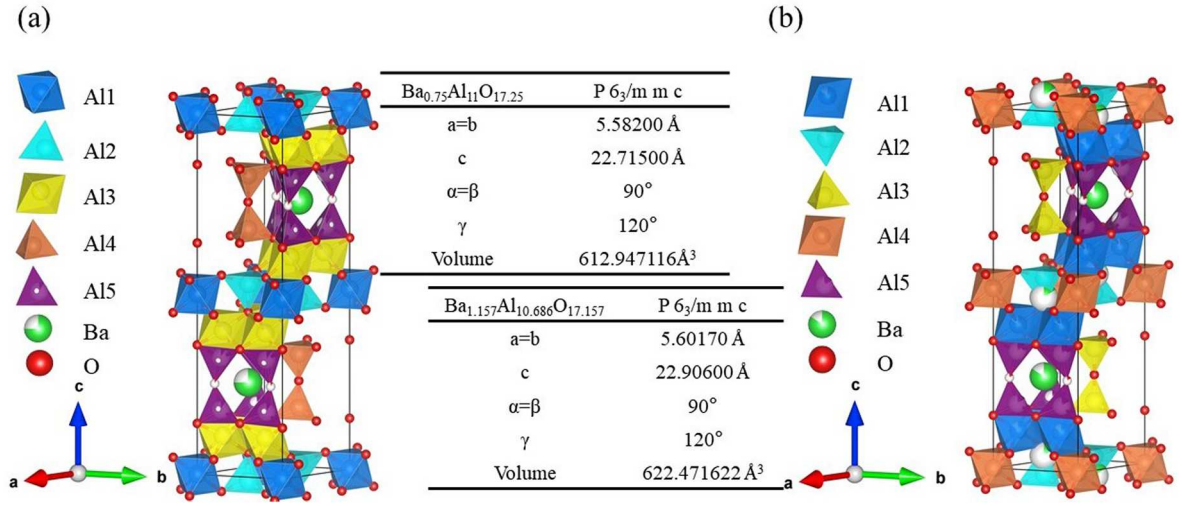

Fig. 2. Crystal structure and lattice parameters of $BaAl_{12}O_{19}$:(a) $Ba_{0.75}Al_{11}O_{17.25}$; (b) $Ba_{1.157}Al_{10.686}O_{17.157}$.

1.1. Crystal structures of oxides in the BaO–Al_2O_3 binary system

The most well-known oxides in the BaO–Al_2O_3 system are $BaAl_{12}O_{19}$ and $BaAl_2O_4$, which contain very high amounts of Al_2O_3. When increasing the amount of BaO, compositions such as $Ba_3Al_2O_6$, $Ba_4Al_2O_7$, $Ba_5Al_2O_8$, and $Ba_7Al_2O_{10}$ appear. However, as Ba (1.50 Å) is much larger in size than Al (0.42 Å) [4], the structures are less stable and easily hydrated or decomposed. Therefore, it is difficult to stabilize compounds with higher Ba ratios with regular synthesis methods. The most recent study on the BaO–Al_2O_3 phase diagram (Fig. 1) is provided based on experimental results and thermal dynamic assessment [9]. The compounds with determined structures are $BaAl_{12}O_{19}$, $BaAl_2O_4$, $Ba_3Al_2O_6$ and $Ba_4Al_2O_7$. The detailed structures of $Ba_5Al_2O_8$ and $Ba_7Al_2O_{10}$ or higher Ba contents remain unclear. As $Ba_5Al_2O_8$ is primarily reported as an impurity phase when synthesizing $Ba_4Al_2O_7$, it will not be discussed here.

1.1.1. $BaAl_{12}O_{19}$

Although barium hexaaluminate (BaO·$6Al_2O_3$) has been described to be monophasic, the β_I Ba-poor phase and β_{II} Ba-rich phase with defective β-Al_2O_3 structures exist [6]. The β_I Ba-poor phase has a composition of $Ba_{0.75}Al_{11}O_{17.25}$, which is derived from sodium β-alumina ($NaAl_{11}O_{17}$) with the *P63/mmc* space group. $NaAl_{11}O_{17}$ is a layered structure arranged along the *c* axis and consists of Al spinel blocks ($Al_{11}O_{16}$) and the so-called mirror layer (NaO) [7]. $Ba_{0.75}Al_{11}O_{17.25}$ is normally treated as a nonstoichiometric compound where 75% of Na^+ ions in $NaAl_{11}O_{17}$ are replaced by Ba^{2+}, while the other 25% of Na^+ are substituted by Ba^{2+} vacancies with nearby interstitial oxygen atoms that are situated at mid-oxygen (mO) sites and act as compensating defects [8]. The Ba-rich β_{II} phase has the formula $Ba_{1.167}Al_{10.667}O_{17.167}$, in which Ba ions are located in both spinel blocks and mirror planes [9]. The detailed structures of $Ba_{0.75}Al_{11}O_{17.25}$ and $Ba_{1.167}Al_{10.667}O_{17.167}$ are shown in Fig. 2. More recently, it has been revealed that a range of hexaaluminate composition groups are nonstoichiometrically in a β-alumina-type structure. Their compositions are summarized as xBaO·$6Al_2O_3$, where x

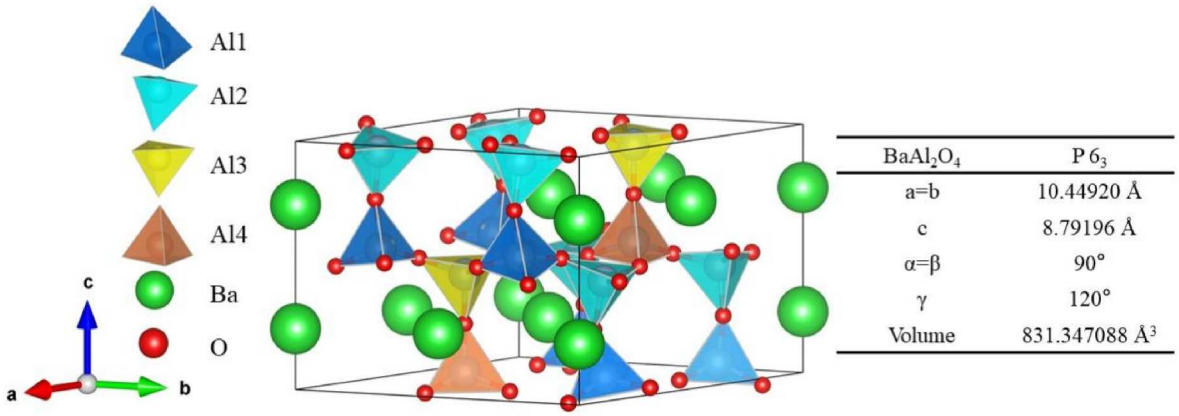

$BaAl_2O_4$	P 6_3
a=b	10.44920 Å
c	8.79196 Å
α=β	90°
γ	120°
Volume	831.347088 Å^3

Fig. 3. Crystal structure and lattice parameters of $BaAl_2O_4$.

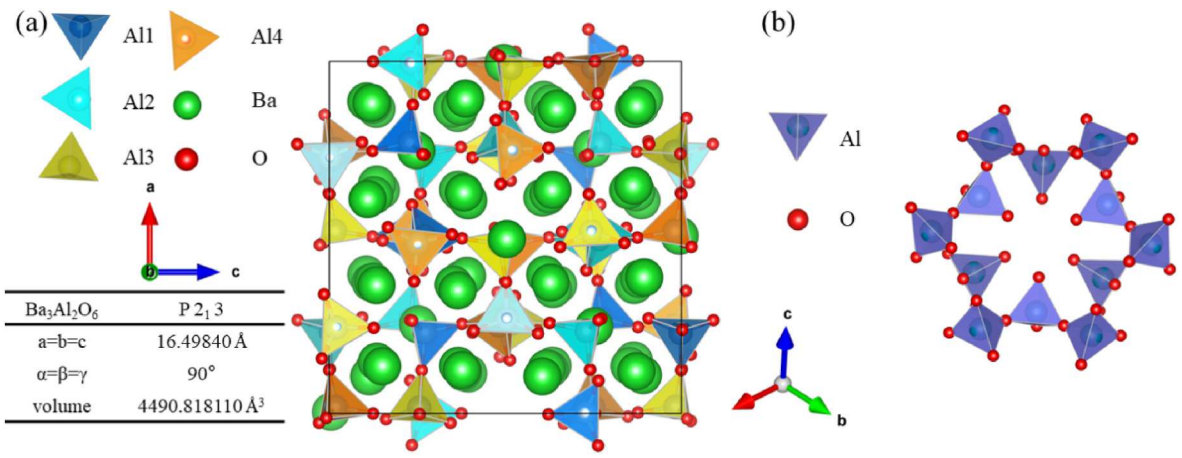

$Ba_3Al_2O_6$	P 2_1 3
a=b=c	16.49840 Å
α=β=γ	90°
volume	4490.818110 Å^3

Fig. 4. The structure of $Ba_3Al_2O_6$: (a) projection of the whole structure of $Ba_3Al_2O_6$ parallel to (010) and lattice parameters; (b) projection of one of the highly wrinkled 12-membered [AlO_4] rings parallel to (111).

extends from 0.80 to 1.32 [10]. Due to the peculiar layered structure consisting of alternative stacking of spinel blocks containing Al^{3+} ions and BaO mirror planes along the *c* axis, Ba-hexaaluminates have high thermal stability [11]. Therefore, it can well meet the requirements of high temperature stability for catalytic combustion and phosphor-converted white light-emitting diodes.

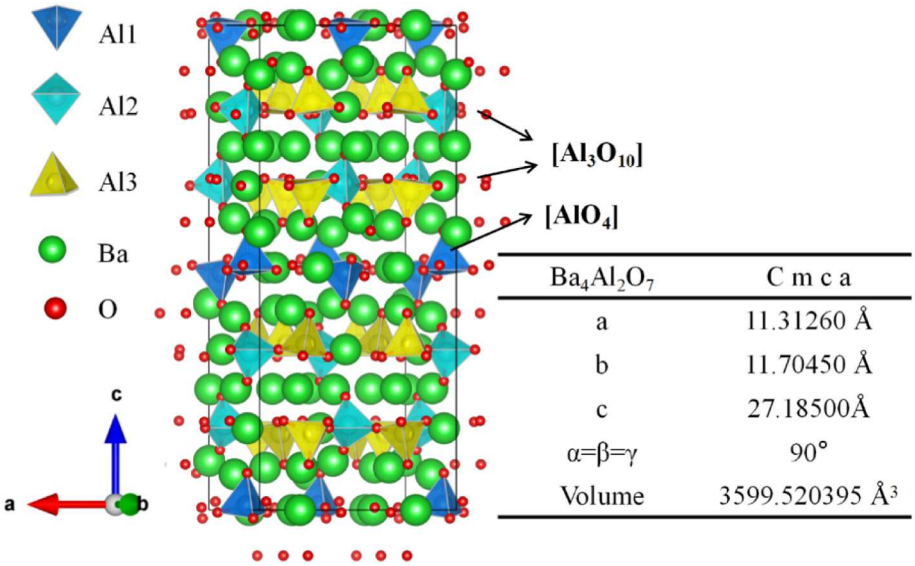

$Ba_4Al_2O_7$	C m c a
a	11.31260 Å
b	11.70450 Å
c	27.18500Å
α=β=γ	90°
Volume	3599.520395 Å^3

Fig. 5. Crystal structure and lattice parameters of $Ba_4Al_2O_7$.

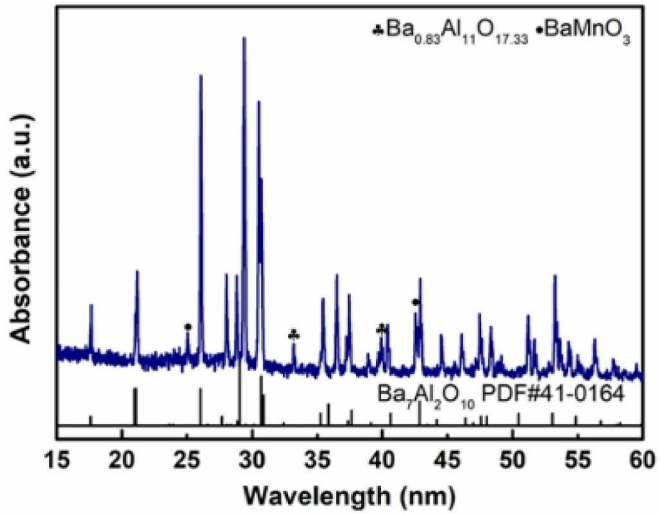

Fig. 6. The XRD patterns of $Ba_7Al_{1.5}Mn_{0.5}O_{10}$ [23].

1.1.2. $BaAl_2O_4$

$BaAl_2O_4$ belongs to a stuffed tridymite-like structure [12], in which large Ba^{2+} ions are situated in the hexagonal channels formed by corner-shared [AlO_4] tetrahedra. There are two hexagonal phases of $BaAl_2O_4$ with a reversible phase transition at 123 °C [13]. At room temperature, the ferroelectric phase with the $P6_3$ space group is observed, while at high temperature, the paraelectric phase with $P6_322$ can be detected. The structure of ferroelectric phase $BaAl_2O_4$ is shown in Fig. 3. Two different Ba sites, Ba1 and Ba2, are located in Wyckoff positions 2a (with C3 symmetry) and 6c (with C1 symmetry) and coordinated by nine O ions and seven O ions, respectively [13]. There are two kinds of [AlO_4] tetrahedra in the structure: the first contains Al_1 and Al_2 atoms with C1 symmetry, constituting an Al–O–Al angle of 156°; the second contains Al_3 and Al_4 atoms with C_{3v} symmetry, forming an Al–O–Al angle close to 180° [13,14].

1.1.3. $Ba_3Al_2O_6$

The structure of $Ba_3Al_2O_6$ adopts the cubic space group $P2_13$, which can be considered a defect perovskite structure. Therefore, the formula is equally expressed as $Ba(Al_{3/4}Ba_{1/8}\square_{1/8})(O_{3/4}\square_{1/4})_3$. The detailed structure is illustrated in Fig. 4. It is difficult to obtain a brief description of the structure because there are nonintersecting threefold symmetry axes of the cubic space group $P2_13$, as seen along the *b* axis (Fig. 4a) [15]. Concerning the coordination environments and the bond valence sums, two groups of barium atoms can be distinguished. Type I Ba is situated in distorted octahedral coordination, and type II Ba is much more irregular. However, focusing on the arrangement of the tetrahedrally and octahedrally coordinated Ba atoms, the structure could be visualized from a stacking of two types of alternating layers perpendicular to the [100] direction. The two layers are connected through shared apical oxygen atoms from the tetrahedra and the octahedra. The remaining barium atoms of type II are incorporated into voids of this framework. The principal structural units of $Ba_3Al_2O_6$ are highly wrinkled 12-membered [AlO_4] rings cross-linked by the Ba cations, which is shown in Fig. 4b.

1.1.4. $Ba_4Al_2O_7$

The $Ba_4Al_2O_7$ crystal belongs to the orthonormal system, *Cmca* space group [16]. As shown in Fig. 5, its main crystal structure unit is the separated [AlO_4] group and the [Al_3O_{10}] group consisting of three corner-sharing [AlO_4] tetrahedra. Seven Ba atoms at different crystallographic sites are located between the cross-linked [AlO_4] and form a Ba–O polyhedron with 6–9 oxygen atoms. Based on the existing studies and phase diagrams, $Ba_4Al_2O_7$ exists stably above 1231 K and belongs to the high-temperature stable phase [5]. For the synthesis of $Ba_4Al_2O_7$, during the cooling process, it is easy to decompose to other compounds, and the pure phase is difficult to obtain. As a result, there are few studies on the application of $Ba_4Al_2O_7$ at present.

1.1.5. $Ba_7Al_2O_{10}$

Since $Ba_7Al_2O_{10}$ is a metastable phase, it is difficult to obtain a single phase compound, and its detailed structural information remains unclear. By doping with Mn in the formula, a much clearer X-ray pattern (Fig. 6) is shown with $Ba_7Al_{1.5}Mn_{0.5}O_{10}$. The major phase and some structural units were analyzed by FTIR and ^{27}Al NMR spectroscopy, leading to some understanding of the structure. As seen in the FTIR spectrum (Fig. 7), the peaks at 878 cm^{-1} and 535 cm^{-1} are attributed to the stretching vibration of [AlO_4] tetrahedra and [AlO_6] octahedra, respectively [1,17–19]. According to the literature, the chemical shifts of [AlO_4] tetrahedra range from +50 ppm to +90 ppm, and those of [AlO_6] octahedra range from 0 ppm to +20 ppm [20–22]. Therefore, the peak at 92.84 ppm is due to the presence of [AlO_4] tetrahedra, while the peak at 15.70 ppm comes from [AlO_6] octahedra, which is consistent with the FTIR spectrum results, indicating the coexistence of [AlO_4] tetrahedra and [AlO_6] octahedra. Due to the existence of a small amount of $Ba_{0.83}Al_{11}O_{17.33}$ in the synthesized samples (seen in Fig. 7), the [AlO_6] octahedra may be derived from the impurity phase $Ba_{0.83}Al_{11}O_{17.33}$ or the major phase $Ba_7Al_2O_{10}$. By comparing the relative strength of the two peaks in the ^{27}Al NMR spectrum, it can be seen that there are a large number of [AlO_4] tetrahedra in the structure of $Ba_7Al_2O_{10}$ and possibly a small number of [AlO_6] sites.

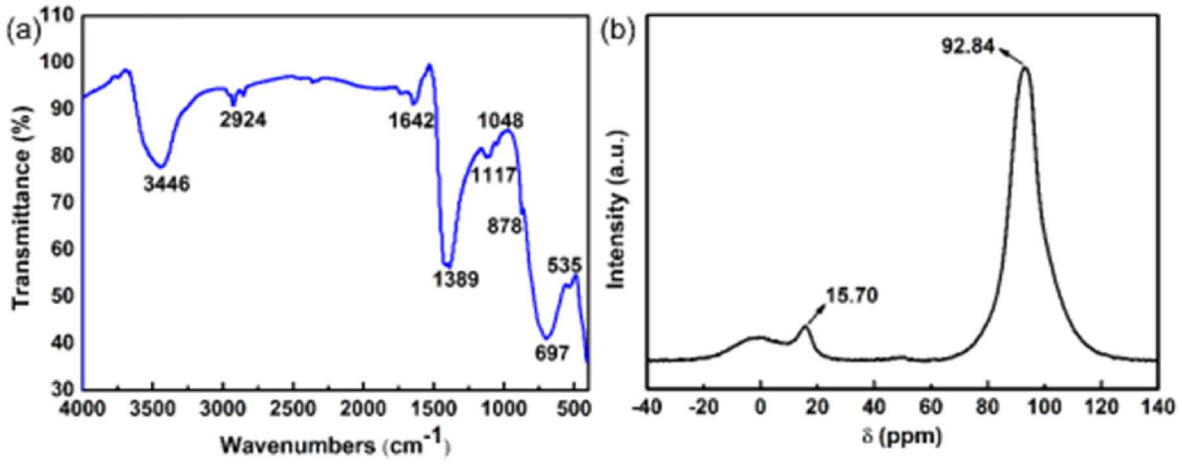

Fig. 7. (a) The FTIR and (b) ^{27}Al NMR of $Ba_7Al_{1.5}Mn_{0.5}O_{10}$ [23].

Table 1
Summary of Eu^{2+} doped in $BaAl_{12}O_{19}$.

Host materials and activator	Synthesis Method	Excitation peak (nm)	Emission peak (nm)	Critical concentration	ref
$BaAl_{12}O_{19}:Eu^{2+}$	Molten salt flux synthesis	350	439	20mol%	[25]
$BaAl_{12}O_{19}:Eu^{2+}$	Solid state reaction	350	447	25mol%	[2]
$BA_{1+x}O:0.2Eu^{2+}$ (x = 1.5)	Solid state reaction	330	450,490	20mol%	[24]
$BaAl_{12}O_{19}:Eu^{2+}$	combustion method	326	444		[26]
$BaAl_{12}O_{19}:Eu^{2+}$	sol–gel method	323	446	10mol%	[27]

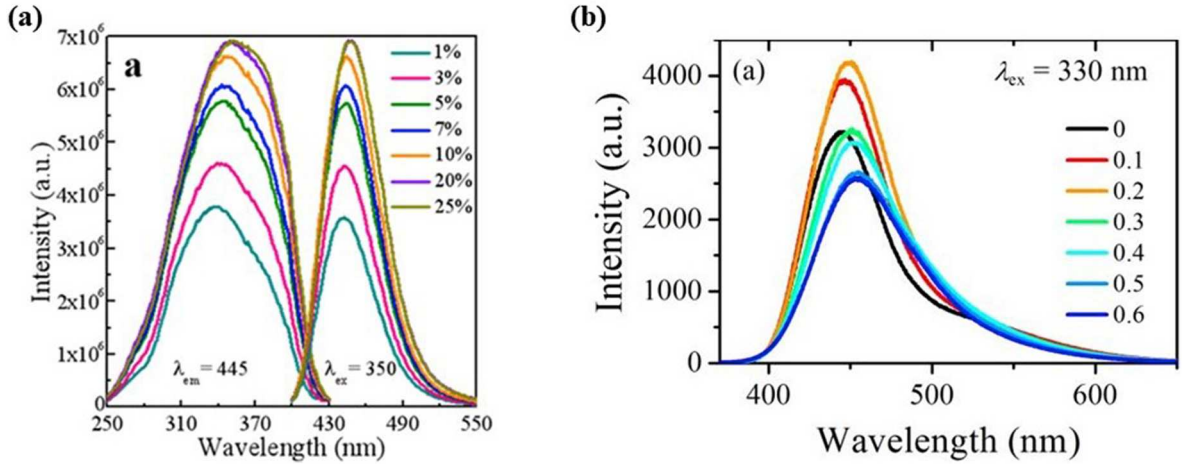

Fig. 8. (a) The photoluminescence excitation (PLE) and emission (PL) spectra of BAO:xEu^{2+} (1% ≤ x ≤ 25%) [2]; (b) PL spectra of $BA_{1+x}O:0.2Eu^{2+}$ (x = 0–0.6, λ_{ex} = 330 nm) [24].

2. Photoluminescent properties

The photoluminescent properties are the most reported optical properties in oxides in $BaO–Al_2O_3$ binary systems. Doping rare earth elements with large and relaxed f orbitals in $BaO–Al_2O_3$ oxides contributes to various color emissions. The majority evaluation of luminescent properties lies in Eu doping in different oxidation states. The luminescence of Eu^{2+} originates from the $4f^7 \rightarrow 4f^6 5d$ transition and usually consists of broad lines. The emission of Eu^{2+} is hypersensitive to the crystal field, as its $5d$ electrons in the excited state are not shielded effectively like the $4f$ electrons in the ground state. As a result, the Eu^{2+} emissions exhibit a broad range from the ultraviolet region to the red region depending on the crystal field of the doped oxide. To date, a large number of Eu^{2+}-doped phosphors have been synthesized with emissions

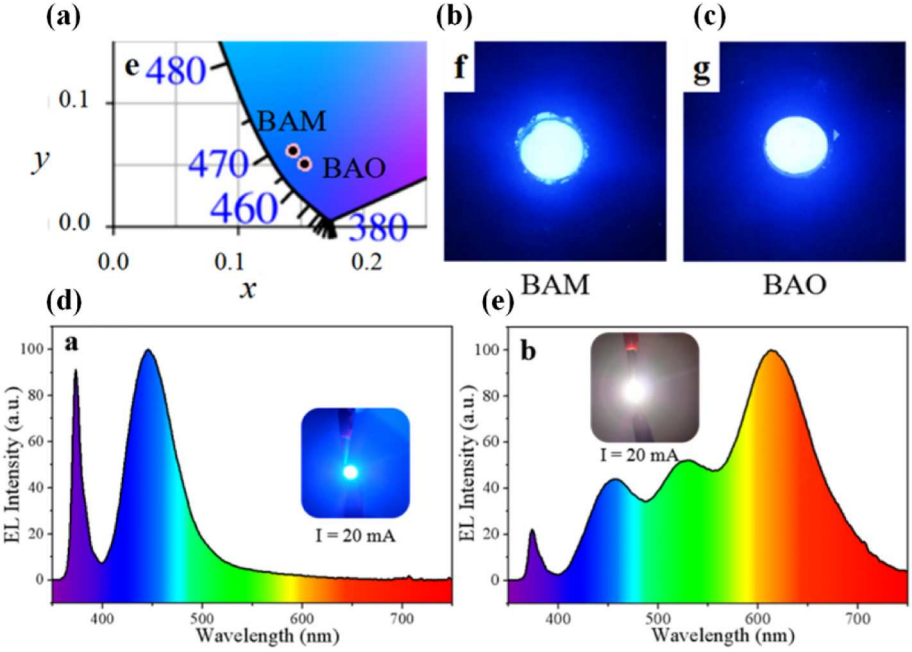

Fig. 9. (a) The CIE chromaticity coordinates diagram of BAM:Eu^{2+} and BAO:25%Eu^{2+}. The luminescence photos of (b) BAM:Eu^{2+} and (c) BAO:25%Eu^{2+} under 365 nm UV light. The electroluminescence spectra and LEDs photograph of (d) BAO:20%Eu^{2+} and (e) BAO:20%Eu^{2+}, $Ba_3Si_6O_{12}N_2:Eu^{2+}$, $CaAlSiN_3:Eu^{2+}$, with 370 nm GaN chip [2].

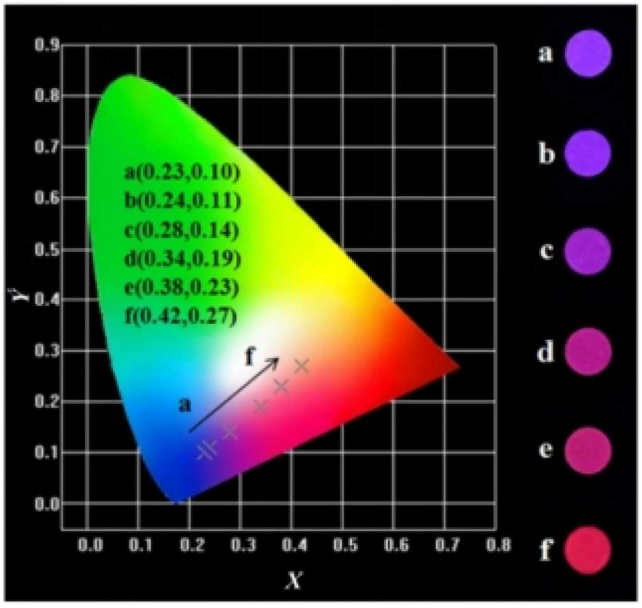

Fig. 10. CIE chromaticity diagram of $Ba_{0.79}Al_{10.9}O_{17.14}$:0.04Eu, yLi^+ (y = 0.04–0.14) [28].

in all visible colors, such as red, orange−yellow, blue and green.

Due to the rare storage of rare earth elements, some transition metal ions with proper oxidation states have also been attempted and succeeded in producing luminescent emissions in BaO–Al_2O_3 oxides. To further control and enhance the luminescent properties, a combination of rare earth metal and transition metal ions is studied in BaO–Al_2O_3 oxides.

2.1. $BaAl_{12}O_{19}$

2.1.1. Rare earth element-doped $BaAl_{12}O_{19}$ phosphors

Due to its facile synthesis, low cost, excellent optical properties, and high physical or chemical stability, Eu^{2+}-activated $BaAl_{12}O_{19}$ has attracted the most research attention for its luminescent properties. Various synthesis methods (Table 1), including traditional high-temperature solid-state reactions [2,24], molten salt flux pathways [25], combustion techniques [26] and sol-gel techniques [27], have been attempted and successfully prepared. A sintering temperature above 1300 °C is necessary to obtain well-crystallized $BaAl_{12}O_{19}$. High-efficiency luminescent materials can be obtained by the traditional high-temperature solid phase method with a simple process and satisfactory production rate.

As stated above, a series of barium hexaaluminate samples can be obtained by adjusting Al/Ba in the range of 9–14 [6]. With the increase in the Al/Ba ratio, the microstructure of compounds changes obviously: the occupancy of Ba^{2+} and cell volume tends to decrease, which would bring about the variation in crystal structure rigidity [24]. Therefore, researchers generally study BaO–Al_2O_3:Eu^{2+} phosphors from two aspects: fixing the Al/Ba ratio and changing the amount of Eu^{2+} doping or doping a certain amount of Eu^{2+} and changing the Al/Ba ratio. $BaAl_{12}O_{19}$:xEu^{2+} (BAO:xEu^{2+}) has a fixed Al/(Ba Eu) ratio. Under an excitation wavelength of 350 nm, $BaAl_{12}O_{19}$:xEu^{2+} (BAO:xEu^{2+}) emits bright blue light consisting of a narrow band from 400 to 525 nm. Its maximum peak position is at approximately 443 nm, as shown in Fig. 8a. In addition, $(Ba_{0.8}Eu_{0.2}O)(Al_2O_3)_{4.575\times(1+x)}$ ($BA_{1+x}O$:$0.2Eu^{2+}$, x = 0.2–0.5) phosphors exhibit a blue−green emission with an emission peak at approximately 450 nm and a shoulder at approximately 490 nm under excitation at 330 nm, as depicted in Fig. 8b. The emission intensity at 150 °C remains more than 90% of that at room temperature. These two kinds of phosphors all show high quantum yields or absolute quantum efficiency.

Comparing the BAO:xEu^{2+} phosphors with $BaMgAl_{10}O_{17}$:Eu^{2+} (BAM:Eu^{2+}), which was commercially used as a blue emitting phosphor, the BAO:xEu^{2+} powders possess a highly pure blue emission, as shown in Fig. 9a. Their photoluminescence under 365 nm UV light in Fig. 9b, c also supports the above statement. To further study its application value, it is assembled into blue LEDs and white LEDs, as shown in Fig. 9d, e. Under a voltage of 3.15 V and a current of 20 mA, the blue LEDs present highly efficient luminescence with a color purity of 87.8% and CIE color coordinates of (0.1578, 0.0769). In addition, the warm white color is garnered with low color temperature (CCT = 3084 K), high color rendering index (Ra = 92.2), and CIE color coordinate of (0.4147, 0.3638). These results suggest that the as-prepared BAO:Eu^{2+} could be an excellent candidate for a blue-emitting phosphor material for application in near-UV-based white LED lighting and displays [2].

The above samples were sintered under a reducing atmosphere (95% N_2 + 5% H_2) to ensure that the doped Eu ions were all in the +2 oxidation state to obtain high blue color purity and emission intensity. In 2017, Wang et al. reported that the reduction of Eu^{3+} to Eu^{2+} occurs in $BaAl_{12}O_{19}$ hosts in air by a reducing agent. The $Ba_{0.79}Al_{10.9}O_{17.14}$:$xEu$ phosphor can be prepared by doping Li^+ ions in air, and the color can be tuned from blue (0.23, 0.10) to red (0.42, 0.27). The emission intensity is maintained at a high level of 70.73% at 150 °C compared with the intensity at room temperature (Fig. 10). Therefore, it may be an alternative selection to obtain color tunable emission for white LEDs [28].

In addition to Eu^{2+}, the other rare earth elements also demonstrate promising luminescent properties in $BaAl_{12}O_{19}$. $BaAl_{12}O_{19}$:Tb^{3+} is a green-emitting phosphor, in which the luminescence originates from $^5D_3 \rightarrow {}^7F_i$ (i = 6, 5, 4, 3) and $^5D_4 \rightarrow {}^7F_j$ (j = 6, 5, 4, 3) transitions in Tb^{3+}. Xiao et al. synthesized $BaAl_{12}O_{19}$:Tb^{3+} phosphors with a λ_{ex} of 240 nm and a λ_{em} of 545 nm via the sol-gel method. It is found that when sintering at 1300 °C for 2 h and with 2 mol% Tb^{3+} in the composition, the emission intensity is the strongest [29]. $BaAl_{12}O_{19}$:Ce^{3+}, Eu^{2+} was also synthesized, and its lifetime was prolonged by the introduction of Ce^{3+} [30].

Codoping of multiple rare earth elements in $BaAl_{12}O_{19}$ will improve the luminescent properties by energy transfer in rare earth elements. Ce^{3+}, Dy^{3+} or Eu^{2+} were successfully introduced into $BaAl_{12}O_{19}$:Tb^{3+}, respectively. For Tb^{3+}/Eu^{2+} $BaAl_{12}O_{19}$, with the concentration of Tb^{3+} fixed at 0.02, the excitation peak shifts from 240 nm to 310 nm by the introduction of Ce^{3+}, as illustrated in Fig. 11a. In Fig. 11b, a characteristic Ce^{3+} emission peak was not observed in the codoped sample. The energy transfer in Ce^{3+} and Tb^{3+} results in an increase in the emission intensity and excitation wavelength range in Ce^{3+}-$BaAl_{12}O_{19}$:Tb^{3+} [31]. In Tb^{3+}/Eu^{2+} codoped $BaAl_{12}O_{19}$ (Fig. 11c), the emission peak of Eu^{2+} at 440 nm is increased, while that of Tb^{3+} at 550 nm is decreased. However, the emission peak intensity of Tb^{2+} at 550 nm is enhanced with the elevated amount of Eu^{2+} in the composition, as illustrated in Fig. 11d. In Dy^{3+}/Eu^{2+} $BaAl_{12}O_{19}$ (Fig. 11e), the emission peaks excited at 291 nm are stronger, and there is no emission peak of Dy^{3+}. In Fig. 11f, the luminescent intensity of Dy^{3+} decreases to zero with increasing Tb^{3+} concentration. Compared with $BaAl_{12}O_{19}$:Tb^{3+}, the Dy^{3+} and Tb^{3+} codoped phosphors are stronger. The above evidence proves the energy delivered between the rare earth elements. The direction of energy delivery can be modified by adjusting their ratio to control the emission light color of phosphors [32,33].

2.1.2. Transition metal ion-doped $BaAl_{12}O_{19}$ phosphors

Transition metal ions, especially Mn, are also doped into $BaAl_{12}O_{19}$ to obtain fluorescent properties. Octahedrally (strong crystal field) and tetrahedrally (weak crystal field) coordinated Mn^{2+} give rise to orange to red emission and green emission, respectively [34,35]. As Mn^{2+} has a high probability of entering tetrahedral vacancies due to the d^5 electronic configuration, Mn^{2+}-doped phosphors always show green emission. $BaAl_{12}O_{19}$:Mn^{2+} green phosphors, with their luminescence raised

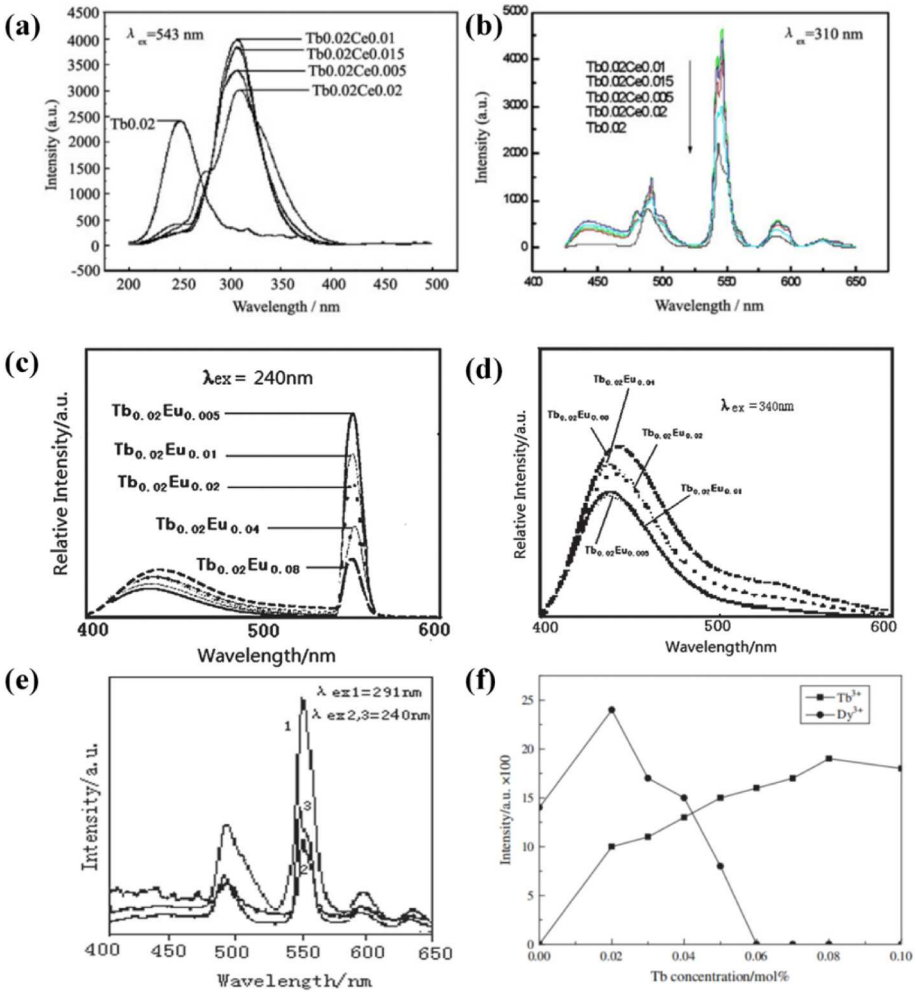

Fig. 11. (a) PLE spectrum of $BaAl_{12}O_{19}$:Tb, Ce at $\lambda_{ex} = 543$ nm; (b) PL spectrum of $BaAl_{12}O_{19}$:Tb, Ce at $\lambda_{ex} = 310$ nm [31]; (c) PL spectrum of $BaAl_{12}O_{19}$:Tb, Eu at $\lambda_{ex} = 40$ nm (d) PL spectrum of $BaAl_{12}O_{19}$:Tb, Eu at $\lambda_{ex} = 340$ nm [32]; (e) PL spectra of $BaAl_{12}O_{19}$:$Tb_{0.08}$, $Dy_{0.02}$ and $BaAl_{12}O_{19}$:$Tb_{0.08}$ ($\lambda_{ex1} = 291$ nm, $\lambda_{ex2,\ 3} = 240$ nm); (f) The emission intensity of Tb^{3+} and Dy^{3+} with Tb^{3+} concentration in $Ba_{1-0.02-x}Al_{12}O_{19}$:$Tb_x$, $Dy_{0.02}$ [33].

Table 2
The summary of $BaAl_{12}O_{19}$:Mn^{2+} phosphor.

Synthesis method	Particle size	Morphology	Ref
solution combustion method	Diameter: 40–100 nm, Length: 200–600 nm	nano-rod morphology	[34, 36]
electrospinning method	Nanoparticle ≤50 nm, Diameter ≈ 400 nm	fibers aggregated by a mass of nanoparticles	[37]
solid-state reaction method	8–10 um	irregular and agglomerate grains	[39]
reverse microemulsion method	40–100 nm	Spherical	[40]
flux assisted solid state re-action method	2–4 μm	regular and fine grains	[35, 41]

from the $3d^5$ ($^4T_1$)-$3d^5$ ($^6A_1$) transition in Mn^{2+}, have a lower decay time, demonstrating advantages as green color sources for plasma display panels (PDPs) [36]. Moreover, $BaAl_{12}O_{19}$:Mn^{2+} phosphors have high luminous efficiency and good stability. Therefore, it is adaptable for field emission displays (FEDs) and Hg-free lamps.

In recent years, $BaAl_{12}O_{19}$:Mn^{2+} studies have focused on enhancing the luminescent intensity and improving its synthesis method [37]. A widely used method to enhance the luminescent intensity of $BaAl_{12}O_{19}$:Mn^{2+} is incorporating other elements. Wang et al. substituted some Al–O bonds with Si–N bonds by introducing Si_3N_4 and SiO_2 into $BaAl_{12}O_{19}$:Mn^{2+}. The lattice parameters were reduced, and therefore, the luminescence intensity of the $BaAl_{12}O_{19}$:Mn^{2+} phosphor was improved [38]. The luminescent intensity is increased by 33.8% by synthesizing S-doped $BaAl_{12}O_{19}$:Mn^{2+} phosphors through a solid-state reaction method [39]. To make the $BaAl_{12}O_{19}$:Mn^{2+} phosphor more suitable for PDPs, various synthetic methods were attempted to adjust its particle size, shape or both (Table 2). Compared with the traditional solid-state method, the electrospinning method reduces the calcination temperature and fabrication of one-dimensional $BaAl_{12}O_{19}$:Mn^{2+} whiskers with a diameter below 50 nm and a length of 400 nm [37]. Similarly, the solution combustion method and reverse microemulsion method can also fabricate nanosized $BaAl_{12}O_{19}$:Mn^{2+} phosphor particles. In addition, the reverse microemulsion method has been proven to decrease its decay time [34,36,40]. H_3BO_3 was added to the $BaAl_{12}O_{19}$:Mn^{2+} phosphor as the flux to promote the solid-state reaction by reducing the sintering temperature. Zhou et al. separately studied the effects caused by a single type of flux and multifold flux synthesis. The addition of flux was proven to reduce the sintering temperature, improve luminescent properties and modify the phosphor morphology [35,41]. The SEM images of the $BaAl_{12}O_{19}$:Mn^{2+} phosphor prepared by the different synthesis methods stated above are shown in Fig. 12.

As Cr^{3+} luminescence is always used in low-cost red-emitting phosphors, it is also doped into $BaAl_{12}O_{19}$ for luminescent purposes. Singh et al. synthesized a $BaAl_{12}O_{19}$:Cr^{3+} phosphor via the combustion method. Its excitation spectrum exhibited characteristic Cr^{3+} bands in distorted octahedral symmetry, resulting in an intense band centered at

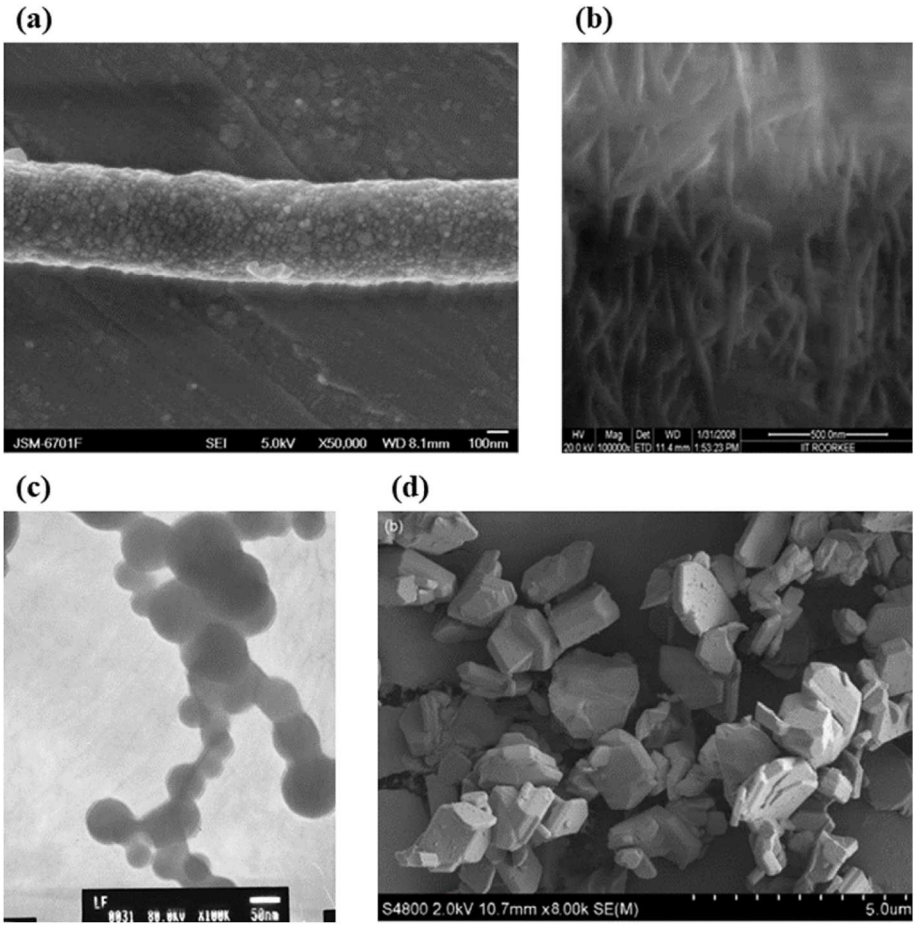

Fig. 12. The SEM images of (a) electrospinning method, (b) solution combustion method, (c) reverse micro-emulsion method, (d) flux assisted solid state reaction method [36,37,40,41].

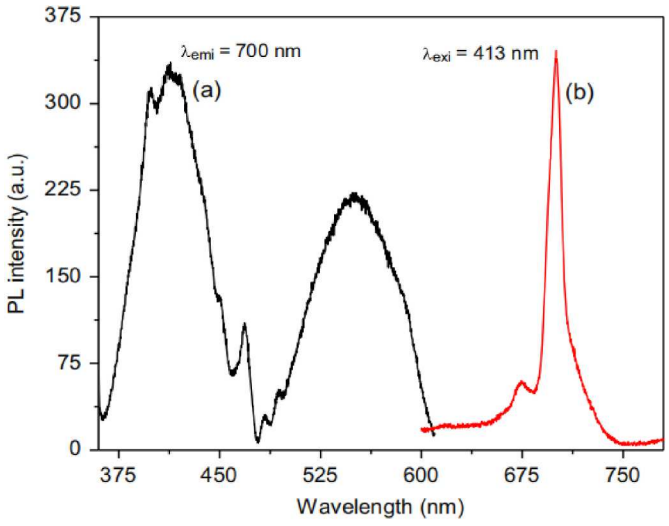

Fig. 13. (a) PLE spectrum (λ_{emi} = 700 nm) and (b) PL spectrum (λ_{exi} = 413 nm) of $BaAl_{12}O_{19}:Cr^{3+}$ [42].

700 nm from the $^2E_g \rightarrow {}^4A_{2g}$ transition (Fig. 13) [42].

2.1.3. *Codoping of Eu^{2+} and a transition metal ion in $BaAl_{12}O_{19}$*

A recent study proved that the luminescence intensity of $BaAl_{12}O_{19}:Eu^{2+}$ could be further enhanced by introducing a transition metal ion that can transfer energy to Eu^{2+}.

The Cr^{3+}-doped $BaAl_{12}O_{19}:Eu^{2+}$ exhibits red emission, which originates from the $^2E \rightarrow {}^4A_2$ transitions of Cr^{3+}. There is no absorption of Cr^{3+} under the 306 nm excitation, but the red emission of Cr^{3+} (at 694 nm and 700 nm) is enhanced with an increase in Cr^{3+} concentrations, indicating an energy transfer existed between Cr^{3+} and Eu^{2+} (Fig. 14a). From Fig. 14b, the emission light color can be controlled by the Cr^{3+} concentration [43]. Singh et al. synthesized blue–green emitting $BaAl_{12}O_{19}:Eu^{2+}$, Mn^{2+} phosphors through a combustion method and confirmed the presence of Eu^{2+} and Mn^{2+} in the $BaAl_{12}O_{19}$ matrix through optical (Fig. 15a) and electron paramagnetic resonance (Fig. 15b) analysis of the sample [44]. The $BaAl_{12}O_{19}:Eu^{2+}$, Mn^{2+} phosphors show blue−green emission, which is due to the emissions of Eu^{2+} at 442 nm and Mn^{2+} at 511 nm.

2.1.4. *$BaAl_{12}O_{19}$ phosphors doped with two ions for dual-mode optical thermometry*

$BaAl_{12}O_{19}$-based phosphors doped with two ions were reported to be applicable for dual-mode optical thermometry, which is sensitive to both the fluorescence intensity and fluorescence lifetime.

In $Mn^{2+}:BaAl_{12}O_{19}–Mn^{4+}:SrAl_{12}O_{19}$, two distinct emission peaks are clearly observed from the excitation spectrum and emission spectrum (Fig. 16). In Fig. 17, the fluorescence lifetime of Mn^{2+} is steadily maintained at different temperatures, while that of Mn^{4+} decays rapidly under temperature variance. Therefore, the $Mn^{2+}:BaAl_{12}O_{19}–Mn^{4+}:SrAl_{12}O_{19}$ solid solution can be used in dual-mode optical thermometry. The coexistence of Mn^{2+} and Mn^{4+} is achieved via the proportion adjustment in solid solution between $BaAl_{12}O_{19}$ and $SrAl_{12}O_{19}$. Mn^{2+} is able to reside in $BaAl_{12}O_{19}$ due to the self-reduction phenomenon by Reidinger defects. Only Mn^{4+} exists in $SrAl_{12}O_{19}$, as there are no

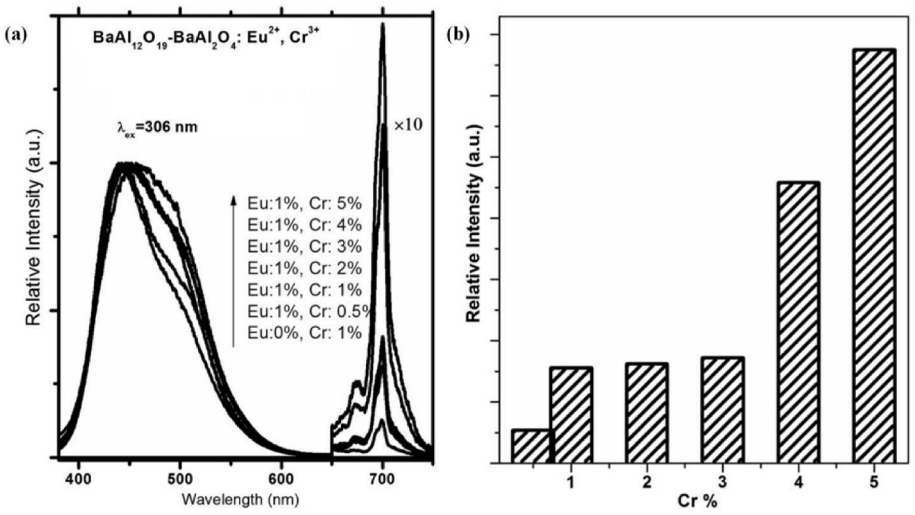

Fig. 14. (a) PL spectra of $BaAl_{12}O_{19}$–$BaAl_2O_4$:1% Eu^{2+}, *x*% Cr^{3+} ($x = 0.5$, 1, 2, 3, 4 and 5 $\lambda_{ex} = 306$ nm). (b) The red/blue emission change with Cr^{3+} concentration variation [43].

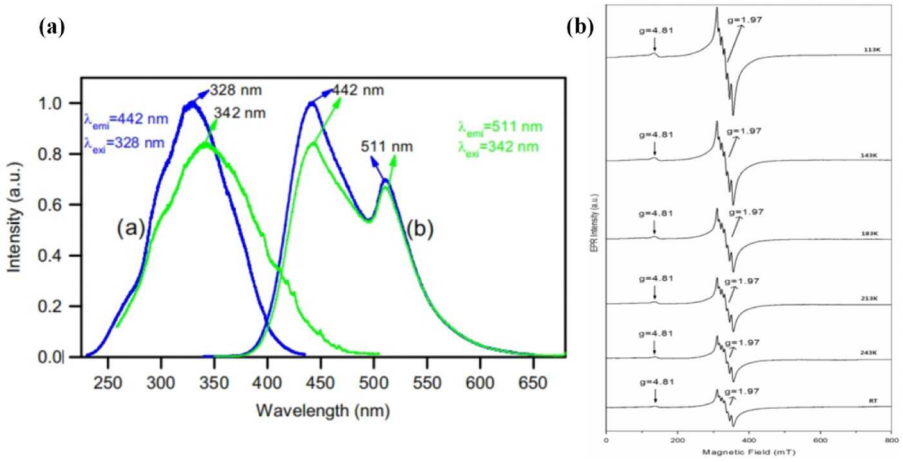

Fig. 15. (a) PLE spectrum for emission at 442/511 nm and PL spectrum for excitation at 328/342 nm of $BaAl_{12}O_{19}$:Eu, Mn; (b) EPR spectra of $BaAl_{12}O_{19}$:Eu, Mn phosphor at different temperatures [44].

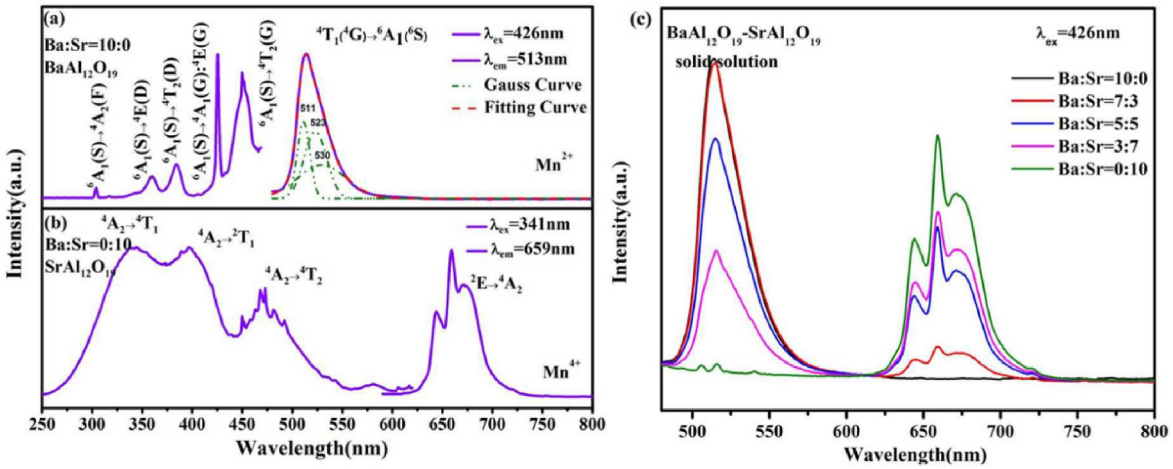

Fig. 16. (a) PLE spectrum and PL spectrum of the host behaves as $BaAl_{12}O_{19}$ pure phase; (b)PLE spectrum and PL spectrum of the host behaves as $SrAl_{12}O_{19}$ pure phase; (c) The PL spectra of the different percentages that Sr^{2+} replacing Ba^{2+} [45].

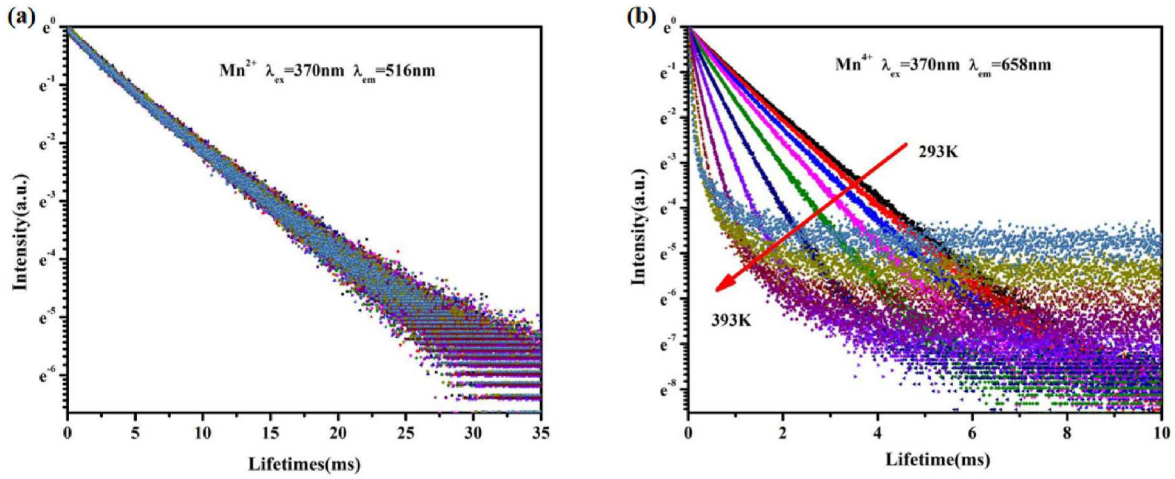

Fig. 17. The $Ba_{0.5}Sr_{0.5}Al_{11.93}O_{19}$:0.07Mn solid solution test the lifetime at variable temperature [45].

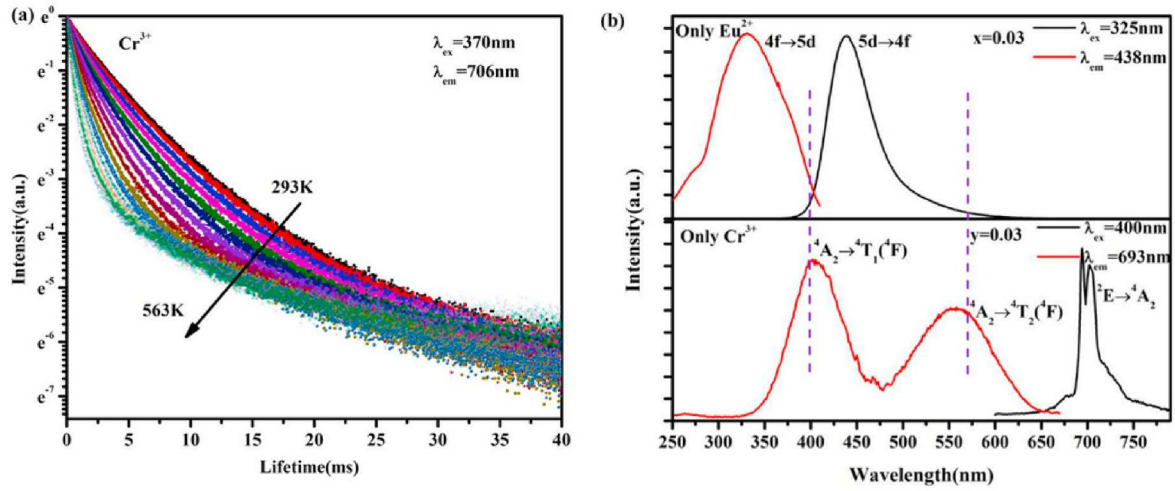

Fig. 18. (a) The fluorescence decay curves of Cr^{3+} emission (λ_{ex} = 370 nm, λ_{em} = 706 nm) in $Ba_{0.97}Al_{11.97}O_{19}$:0.03$Eu^{2+}$, 0.03$Cr^{3+}$ phosphors at different temperatures; (b) PLE and PL spectra of $Ba_{0.97}Al_{12}O_{19}$:0.03Eu^{2+} and $BaAl_{11.97}O_{19}$:0.03Cr^{3+} [46].

Reidinger defects [45].

As stated above, $BaAl_{12}O_{19}$:Eu^{2+}, Cr^{3+} is used for illumination and displays excellent photoluminescent properties. In addition, Cr^{3+} has high temperature sensitivity to the fluorescence lifetime. The emissions of Eu^{2+} ions and Cr^{3+} ions can be well separated, which can provide excellent signal recognition capabilities for dual-mode optical thermometry (Fig. 18). Moreover, the energy transfer from Eu^{2+} to Cr^{3+} strengthens the fluorescence intensity of Cr^{3+}, which provides convenience for expanding the thermometry range [46]. Therefore, $BaAl_{12}O_{19}$:Eu^{2+}, Cr^{3+} is also a potential material for dual-mode optical thermometry.

2.2. $BaAl_2O_4$

2.2.1. Rare earth element-doped $BaAl_2O_4$ phosphors

Similar to $BaAl_{12}O_{19}$, rare earth elements are also successfully doped into $BaAl_2O_4$ to pursue luminescent properties.

Eu doped in $BaAl_2O_4$ exhibits two oxidation states, +3 and + 2. $BaAl_2O_4$:Eu^{3+}, which is utilized extensively in numerous commercial applications ranging from display to solid-state lighting, is currently one of the most achieved high-quality red phosphors. Its quantum efficiency of luminescence evidently decreased with annealing temperature. The Pechini method and sol-gel method are well developed to synthesize $BaAl_2O_4$:Eu^{3+} phosphors. The Pechini method normally leads to a higher intrinsic emission quantum yield and higher emission color purity of the as-prepared phosphor [47].

When Eu^{2+} is introduced into $BaAl_2O_4$, it will occupy Ba positions, which are surrounded by 9 oxygen atoms. There are two Ba^{2+} ion sites (2a and 6c) in the $BaAl_2O_4$ structure, and one of them produces an emission at 495 nm, while the other gives rise to an emission at 530 nm. Therefore, $BaAl_2O_4$:Eu^{2+} exhibits green emission because of the $4f^7$-$4f^65d$ transitions in Eu^{2+} ions [48]. Nakauchi et al. compared $BaAl_2O_4$ doped with different concentrations of optically active Eu^{2+} ions and concluded that a 3% Eu^{2+}-doped sample showed the highest quantum yield and scintillation light yield and the lowest afterglow [49].

The persistent luminescent phenomenon is currently understood to relate to the electrons trapped and released by traps [50]. Thus, the number and depth of the traps have an inseparable relationship with the persistent luminescence phenomenon, which directly affects the length of the afterglow [51]. In $BaAl_2O_4$:Eu^{2+}, R^{3+}, the electrons in Eu^{2+} are excited from the 4*f* ground state to the 5d level. Some of them escape to the conduction band after irradiation and become trapped from there by rare earth codopants, neighboring crystal vacancies or both [51–53]. The energy of persistent luminescence is stored in traps.

As inferred from Fig. 18, the types of R^{3+} and temperature can affect the persistent luminescent phenomenon. In $BaAl_2O_4$:Eu^{2+}, R^{3+}, the

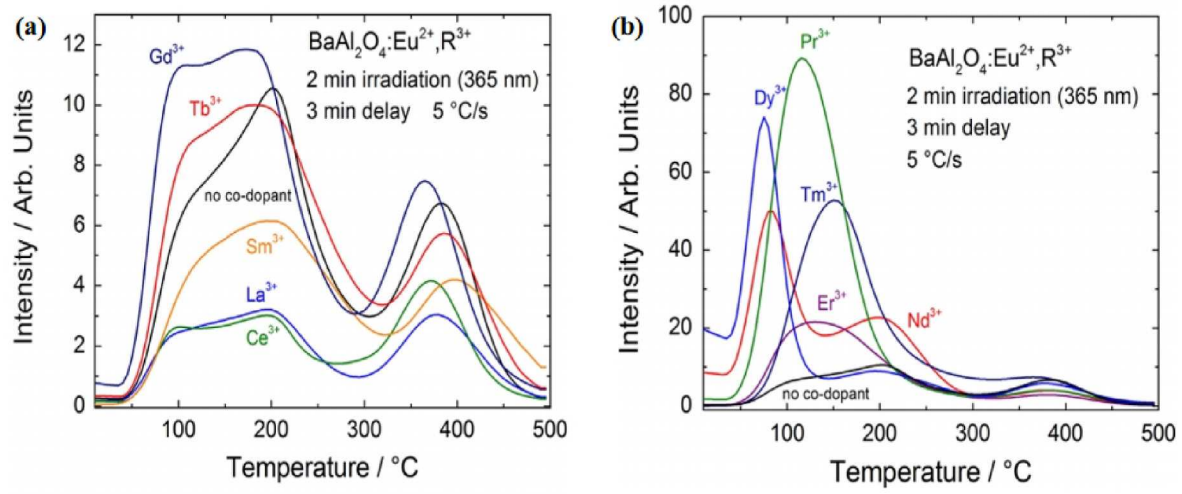

Fig. 19. Thermoluminescence glow curves of $BaAl_2O_4:Eu^{2+}$, R^{3+} (R: (a) none, La, Ce, Sm, Gd and Tb and (b) none, Pr, Nd, Dy, Er and Tm) [55].

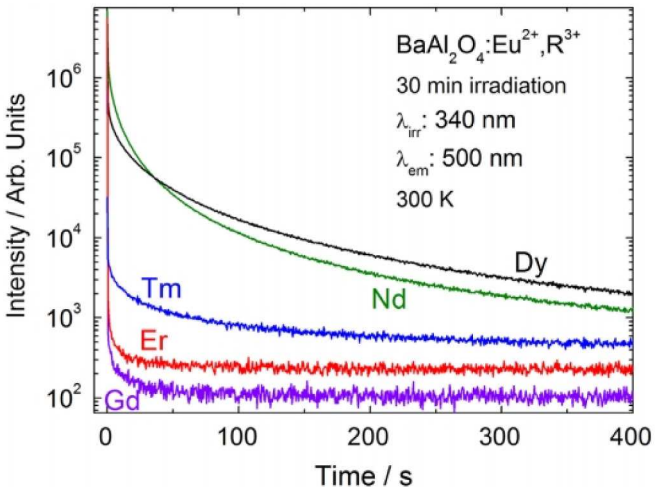

Fig. 20. The persistent luminescence decay curves of selected $BaAl_2O_4:Eu^{2+}$, R^{3+} [55].

materials codoped with La^{3+}, Ce^{3+}, Sm^{3+}, Gd^{3+} and Tb^{3+} have low concentrations of defects. Therefore, it is difficult to find a persistent luminescence phenomenon after irradiation, and the thermoluminescence intensity is low (Fig. 19a). The materials codoped with Pr^{3+}, Er^{3+} and Tm^{3+} exhibit higher maximum luminescence intensity values, but their peak positions are located above 100 °C, which is not applicable for ambient conditions (Fig. 19b). $BaAl_2O_4$ codoped with Nd^{3+} or Dy^{3+} shows a higher thermoluminescence intensity at room temperature. It was also proven that only Nd^{3+} or Dy^{3+} codoped materials have elevated concentrations of defects with a longer duration of persistent luminescence (Fig. 20) [54,55].

Dy^{3+} is used more widely than Nd^{3+}. Eu^{2+}, Dy^{3+} codoped $BaAl_2O_4$, as a completely new generation of persistent luminescent phosphors, has excellent luminescent properties, such as high luminescent intensity, high quantum efficiency and long-lasting afterglow. Its chemical stability is also more satisfactory than that of traditional phosphors. Different synthesis methods have also been used to further promote the properties of $BaAl_2O_4:Eu^{2+}$, Dy^{3+}. Homogeneous coprecipitation, hydrothermal-homogeneous precipitation, and combustion synthesis assisted by microwave irradiation were all reported to succeed in the preparation of $BaAl_2O_4:Eu^{2+}$, Dy^{3+}, demonstrating improvements in particle morphology, emission intensity or afterglow [56–59]. Modification in the doping concentration of Dy^{3+}, substitution of Ba by Sr or

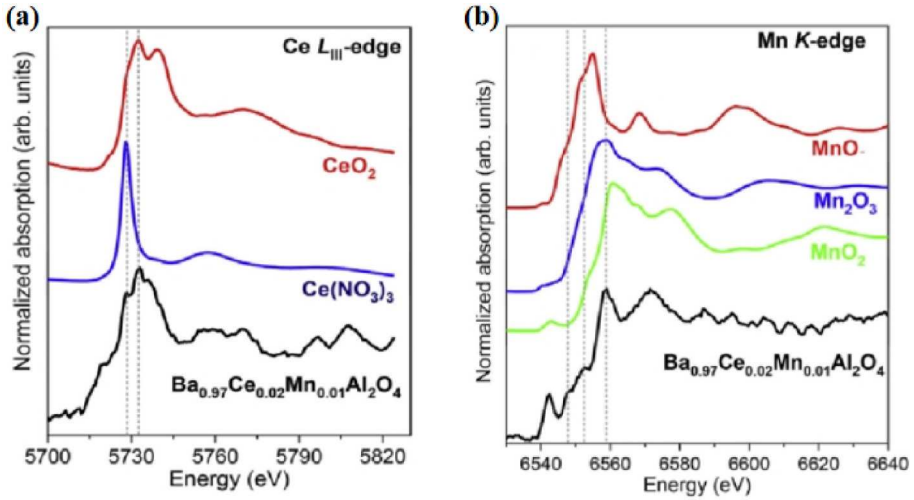

Fig. 21. The XANES spectra of (a) $Ba_{0.97}Ce_{0.02}Mn_{0.01}Al_2O_4$, and standard Ce references Ce^{3+} and Ce^{4+}; and (b) $Ba_{0.97}Ce_{0.02}Mn_{0.01}Al_2O_4$, and standard Mn references Mn^{2+}, Mn^{3+} and Mn^{4+} [70].

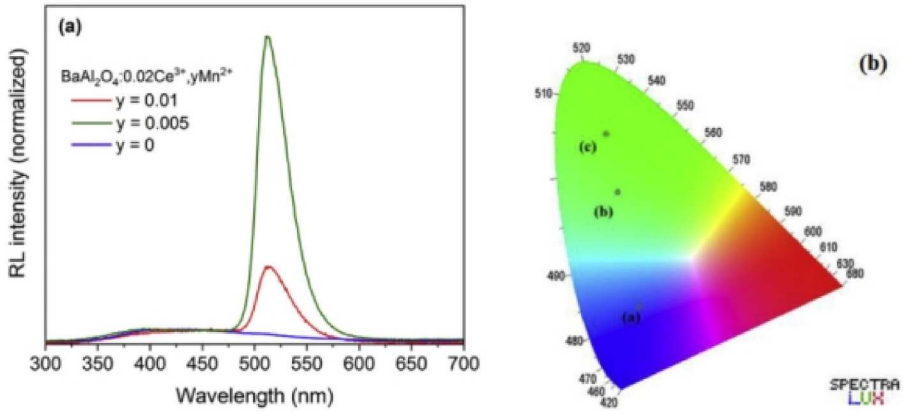

Fig. 22. (a) Radioluminescent spectra of $BaAl_2O_4$:0.02Ce^{3+}, yMn^{2+} ($y = 0$, 0.005 and 0.01); (b) CIE chromaticity diagram of $BaAl_2O_4$:0.02Ce^{3+}, $BaAl_2O_4$:0.02Ce^{3+}, 0.01Mn^{2+} and $BaAl_2O_4$:0.02Ce^{3+},0.005Mn^{2+} [70].

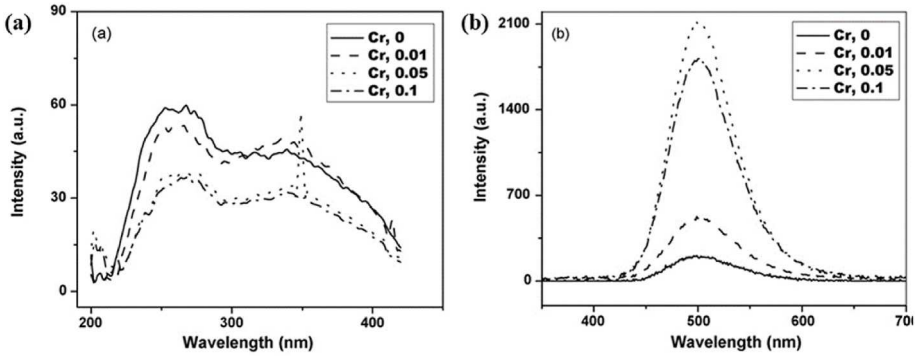

Fig. 23. (a) PLE spectra and (b) PL spectra for $BaAl_2O_4$:Eu^{2+}, Cr^{3+} (0, 0.01, 0.05, 0.1 mol% Cr) [71].

addition of Li_2CO_3 into the $BaAl_2O_4$:Eu^{2+}, Dy^{3+} phosphor will also help [60–64].

In addition to Eu, other rare earth elements, such as Tb^{3+} and Ce^{3+}, also show good photoluminescent properties. $BaAl_2O_4$:Tb^{3+} shows the green emission produced by the $^5D_4 \rightarrow {}^7F_j$ ($j = 0$–6) transitions of Tb^{3+} upon UV excitation. With the increase in Tb^{3+} doping concentration, the luminescence lifetime also increases [65]. The cost-effective sol-gel method is employed to synthesize Tb^{3+}-doped $BaAl_2O_4$ nanophosphors. Ce^{3+}-doped $BaAl_2O_4$ synthesized by the sol-gel method shows bright blue emission that is due to the $5d \rightarrow 4f$ transitions of Ce^{3+}. Owing to promising color purity, thermal quenching and antiaging properties, the phosphor can potentially be applied in solid-state lighting and field-emission display devices [66].

2.2.2. *Transition metal ion-doped $BaAl_2O_4$ phosphors*

In Mn-doped $BaAl_2O_4$, Mn ions can exist as Mn^{2+} and Mn^{4+}. The green luminescence of $BaAl_2O_4$:Mn^{2+} suggests that Mn^{2+} probably occupies a tetrahedral site in $BaAl_2O_4$. The luminescence of Mn^{2+} is rooted in the $^4T_1$ (^4G)-$^6A_1$ (^6S) transition, and its decay time is in milliseconds without persistent luminescence [67]. The luminescence of Mn^{4+} is rooted in the $^2E \rightarrow {}^4A_2$ transition, showing red emission. $BaAl_2O_4$:Mn^{4+} is synthesized by the urea combustion method, which is facile and economically viable [68].

$BaAl_2O_4$:x% Cu^{2+} ($0 \leq x \leq 1$) has a bluish emission color, so it can be an alternative oxide phosphor for blue light emitting diodes (BLEDs). Maphiri et al. concluded that the excitation wavelength and Cu^{2+} concentration can affect its blue color emission. The optimum Cu^{2+} concentration and critical energy transfer distance (Rc) were proven to be 0.075% Cu^{2+} and 12.01 Å, respectively [69].

2.2.3. *Codoping of rare earth elements and metal ions in $BaAl_2O_4$*

In Mn and Ce codoped $BaAl_2O_4$, Ce exists in the form of Ce^{3+} and Ce^{4+}, while Mn exists in the form of Mn^{3+} and Mn^{4+}. There is a possibility that Mn^{2+} is also present as a minor group based on the XANES curves shown in Fig. 21. A change in the concentration of the codoped Mn ion will also modify the emission color (Fig. 22) [70].

When Cr^{3+} is doped into $BaAl_2O_4$:Eu^{2+}, the phosphor exhibits green emission due to the $4f^6 5d^1 \rightarrow 4f^7$ transition in Eu^{2+}. Cr^{3+} doping leads to the long persistence of the phosphor by creating deep traps to prolong the relaxation of these secondary ions. From Fig. 23, a higher emission efficiency was observed for the Cr-doped samples compared to the parent phosphor without Cr [71]. Ti^{3+} behaves the same as Cr^{3+} when incorporated into $BaAl_2O_4$:Eu^{2+}, contributing to the improvement of emission efficiency [72].

Some researchers have also doped K^+ ions or Ca^{2+} ions to improve the luminescent property of $BaAl_2O_4$:Eu^{2+}. Due to K^+ codoping, the better crystallinity contributes to an increase in luminescence intensity. The inter-Eu distance was also elongated, which prolongs the radiative lifetime by reducing various nonradiative transitions and electron-phonon coupling strengths [47].

2.3. *$Ba_3Al_2O_6$ and $Ba_4Al_2O_7$*

Compared with $BaAl_{12}O_{19}$ or $BaAl_2O_4$, $Ba_3Al_2O_6$ and $Ba_4Al_2O_7$ are less covered due to stability concerns. $Ba_7Al_2O_{10}$ is a metastable phase, and currently, there is no research coverage on its application potential in phosphors.

The structure of $Ba_3Al_2O_6$ belongs to the cubic system with space group $Pa3$, and Ba has six independent crystallographic sites in $Ba_3Al_2O_6$ lattices, which is an advantage as a parent compound for phosphor

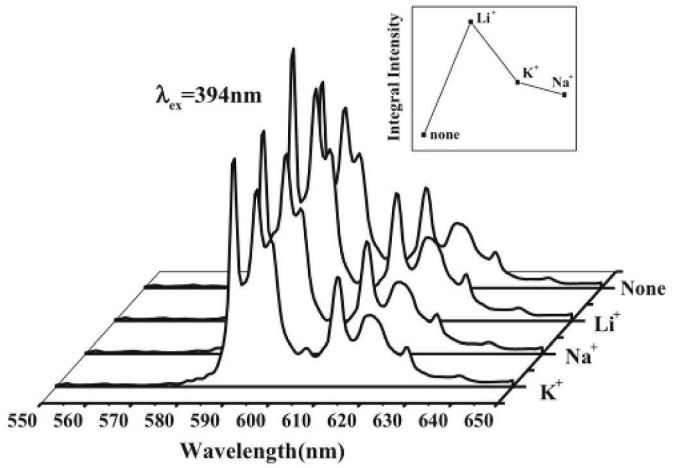

Fig. 24. The PL spectra of $Ba_3Al_2O_6$:0.06Eu^{3+} samples doped with different charge compensators (λ_{ex} = 394 nm) [73].

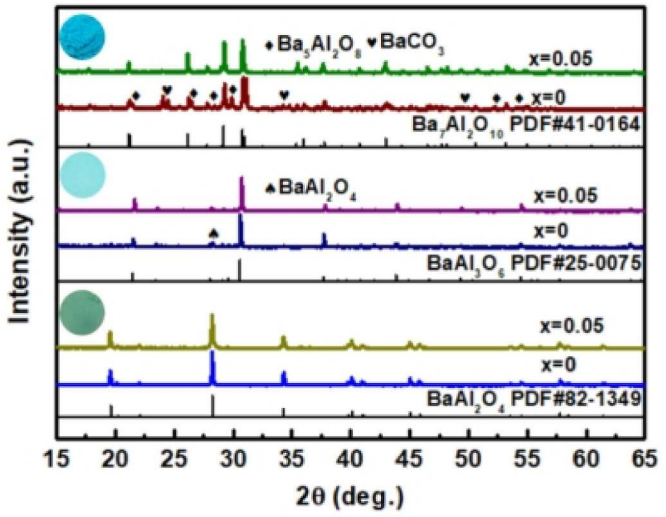

Fig. 25. The XRD patterns of $BaAl_{2-x}Mn_xO_4$, $Ba_3Al_{2-x}Mn_xO_6$ and $Ba_7Al_{2-x}Mn_xO_{10}$ ($0 \le x \le 0.05$).

research [73]. You et al. synthesized a $Ba_3Al_2O_6$:Eu^{3+} phosphor by a high-temperature solid-state method and found that a higher calcination temperature leads to better crystallinity. $Ba_3Al_2O_6$:Eu^{3+} shows red emission from the $^5D_0 \rightarrow {}^7F_1$ transition of Eu^{3+}. With the increase in Eu^{3+} concentration, the impurity phase $BaAl_2O_4$ will appear. To reduce the distortion of local symmetries of optical centers, researchers introduce Li^+, Na^+ and K^+ for charge compensation. Li^+-$Ba_3Al_2O_6$:Eu^{3+} exhibits the strongest emission intensity (Fig. 24) [73].

Eu^{2+}- and Dy^{3+}-doped $Ba_4Al_2O_7$ phosphors were synthesized by the combustion method. $Ba_4Al_2O_7$:Eu^{2+} shows bluish-green emission from the $4f^65d^1 \rightarrow 4f^7$ transition in Eu^{2+}. $Ba_4Al_2O_7$:Dy^{3+} has two emission bands with one centered at 478 nm (blue) and another at 575 nm (yellow). $Ba_4Al_2O_7$:Eu^{2+} and $Ba_4Al_2O_7$:Dy^{3+} show potential in solid-state lighting due to their luminescent properties [74].

3. Visible color

Zhou et al. reported that a turquoise-green color can be obtained when introducing Mn^{5+} into $BaAl_2O_4$ [75]. Producing intense colors by Mn^{5+}-doped tetrahedral coordination in $BaO–Al_2O_3$ compounds also attracts research focus. According to the literature, Mn^{5+} is usually not stable in oxides. However, it can be stabilized in tetrahedral coordination sites of oxides with Ba^{2+}. Mn^{5+}-doped $Ba_3Al_2O_6$ presented sky blue to ocean blue, while cyan to ocean blue can be obtained when Mn^{5+} is hosted at Al^{3+} tetrahedral sites in $Ba_7Al_2O_{10}$. Unfortunately, Mn^{5+}-doped $BaAl_2O_4$ requires a complex sol-gel synthesis, and the doping amount of Mn is lower, so its application is limited. Co^{2+} or Ni^{2+}-doped $BaAl_{12}O_{19}$ presents an intense blue color with high chemical stability and can be used as a ceramic dyeing agent. These discoveries greatly enriched the research content in the field of $BaO–Al_2O_3$ system performance and extended the application scope.

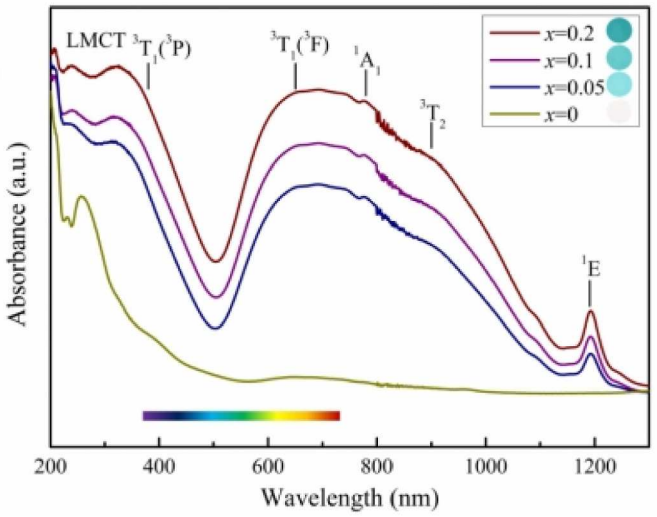

Fig. 26. UV–Vis absorbance spectrum of $Ba_3Al_{2-x}Mn_xO_{6+y}$ ($0 \le x \le 0.2$) [76].

3.1. Mn^{5+}-doped $BaAl_2O_4$, $Ba_3Al_2O_6$ and $Ba_7Al_2O_{10}$

Representative X-ray diffraction patterns of Mn^{5+}-doped $BaAl_2O_4$, $Ba_3Al_2O_6$ and $Ba_7Al_2O_{10}$ are shown in Fig. 25. $BaAl_2O_4$ is a hexagonal phase of the $P6_3$ space group, and $Ba_3Al_2O_6$ belongs to the cubic phase of the $P2_13$ space group. The pure $Ba_7Al_2O_{10}$ phase is difficult to synthesize, as its structure has not been determined, but the introduction of Mn is beneficial to the stability of $Ba_7Al_2O_{10}$.

The oxidation state of Mn was confirmed by X-ray photoelectron spectroscopy. The binding energies of Mn in $BaAl_{1.95}Mn_{0.05}O_{4+y}$, $Ba_3Al_{1.9}Mn_{0.1}O_6$ and $Ba_7Al_{1.5}Mn_{0.5}O_{10}$ are 642.3 eV, 642.43 eV and 642.43 eV, receptively [23,75,76]. The results are well inside the range expected for the binding energy of Mn^{5+} in tetrahedral coordination by comparison with Mn^{5+} in $Ba_2In_{2-x}Mn_xO_5$ (642.75 eV) [77] and $Ca_6Ba(P_{1-x}Mn_x)_4O_{17}$ (642.8 eV) [78]. Further study of its UV–Vis absorption spectrum showed that the coloration of the compounds depended on the allowed *d-d* transition of Mn^{5+}, whose peaks were in the visible to infrared range. The absorbance peaks produced by the Al–O and Mn–O ligand-to-metal charge-transfer (LMCT) transition are in the UV region, which has little effect on the hues of the compounds. As seen in Fig. 26, there are five transitions of $3d^2$ of $[Mn^{5+}O_4]$ groups in the low-symmetry (C_{3v}) tetrahedral field, including three spin allowed absorptions $^3A_2 \rightarrow {}^3T_1(^3P)$ (380 nm), $^3A_2 \rightarrow {}^3T_1(^3F)$ (650 nm) and $^3A_2 \rightarrow {}^3T_2$ (900 nm) transitions and two spin forbidden absorptions $^3A_2 \rightarrow {}^1A_1$ (780 nm) and $^3A_2 \rightarrow {}^1E$ (1200 nm) transitions. With the increase in Mn content, the absorption peaks at approximately 400 nm and 600–800 nm become stronger and broader, resulting in a decrease in the sample brightness. The colors of the compounds are tuned from sky blue to turquoise (Fig. 27).

All three compounds ($BaAl_{2-x}Mn_xO_4$, $Ba_3Al_{2-x}Mn_xO_6$ and $Ba_7Al_{2-x}Mn_xO_{10}$) exhibit similar UV–Vis absorbance spectra. Further study on the color of the three solid solutions found that with increasing Ba content, the maximum doping amount of manganese and the blue value all increased.

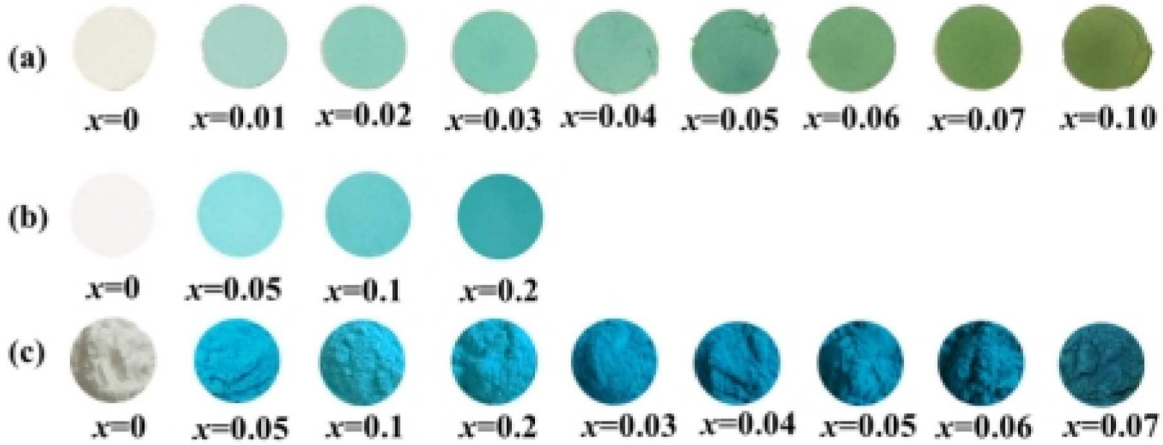

Fig. 27. The apparent colors of (a) $BaAl_{2-x}Mn_xO_{4+y}$ ($0 \leq x \leq 0.1$); (b) $Ba_3Al_{2-x}Mn_xO_{6+y}$ ($0 \leq x \leq 0.2$); (c) $Ba_7Al_{2-x}Mn_xO_{10+y}$ ($0 \leq x \leq 0.7$).

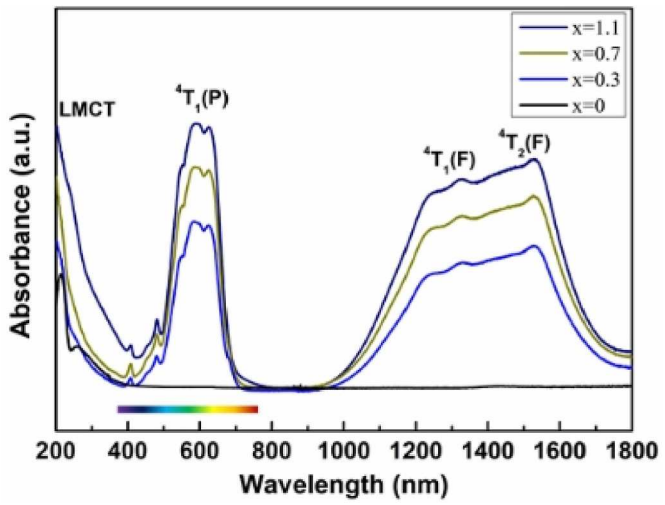

Fig. 28. The absorbance spectrum of $BaAl_{12-x}Co_xO_{19+y}$ ($0 \leq x \leq 1.1$) [81].

3.2. Co^{2+} or Ni^{2+}-doped $BaAl_{12}O_{19}$

By introducing Co^{2+} or Ni^{2+} in $BaAl_{12}O_{19}$, solid solutions of $BaAl_{12-x}Co_xO_{19}$ and $BaAl_{12-x}Ni_xO_{19}$ with royal blue and sky blue colors were synthesized through a solid-state reaction. The absorbance spectrum of $BaAl_{12-x}Co_xO_{19}$ inferred that Co^{2+} is located in tetrahedral coordination. There are three spin-allowed d-d transitions of 3 d^7 ions in $[Co^{2+}O_4]$, including $^4A_2$ (F) → $^4T_1$ (P) (550–750 nm), $^4A_2$ (F) → $^4T_1$ (F) (1320 nm) and $^4A_2$ (F) → $^4T_2$ (F) (1520 nm) (Fig. 28) [79,80].

As seen from the absorption spectrum of $BaAl_{12-x}Ni_xO_{19}$ (Fig. 29), there are three strong optical absorptions in 200–400 nm, 500–800 nm and 100–1200 nm. According to the fitting of the Kubelka-Munk absorption spectrum of $BaAl_{11.7}Ni_{0.3}O_{19}$ bands, the absorption peaks are rooted in the Ni–O ligand-to-metal charge-transfer (LMCT) and the *d-d* transitions of 3 d^8 ions in tetrahedral and octahedral coordination. In Fig. 29, there are three spin-allowed transitions in the $[Ni^{2+}O_4]$ groups: $^3T_1$ (^3F)→$^3T_2$ (^3F) (4438 cm^{-1}), $^3T_1$ (^3F)→$^3A_2$ (^3F) (8665 cm^{-1}) and $^3T_1$ (^3F)→$^3T_1$ (^3P) (15000 cm-1-19000 cm^{-1}), in which $^3T_1$ (^3F) is a ground state. The $^3T_1$ (^3F)→$^3T_1$ (^3P) transition undergoes a splitting in two terms of $^3A_2$ and ^3E due to the lower tetrahedral symmetry. Weaker bands are related to spin-forbidden transitions from $^3T_1$ (^3F) to $^1T_2$ (^1D), ^1E (^1D), $^1T_2$ (^1G), $^1A_1$ (^1G) and $^1T_1$ (^1G) (bands 4, 5, 9–11 in Fig. 29a), respectively. Only a small amount of Ni^{2+} is introduced into the octahedral sites according to the weaker bands of the $^3A_2$ (^3F)→$^3T_{2g}$ (^3F) transition and $^3A_2$ (^3F)→$^3T_{1g}$ (^3F) transition [81–83].

4. Catalytic properties

4.1. Catalytic properties of $BaAl_{12}O_{19}$

$BaAl_{12}O_{19}$ is considered a candidate catalyst for methane

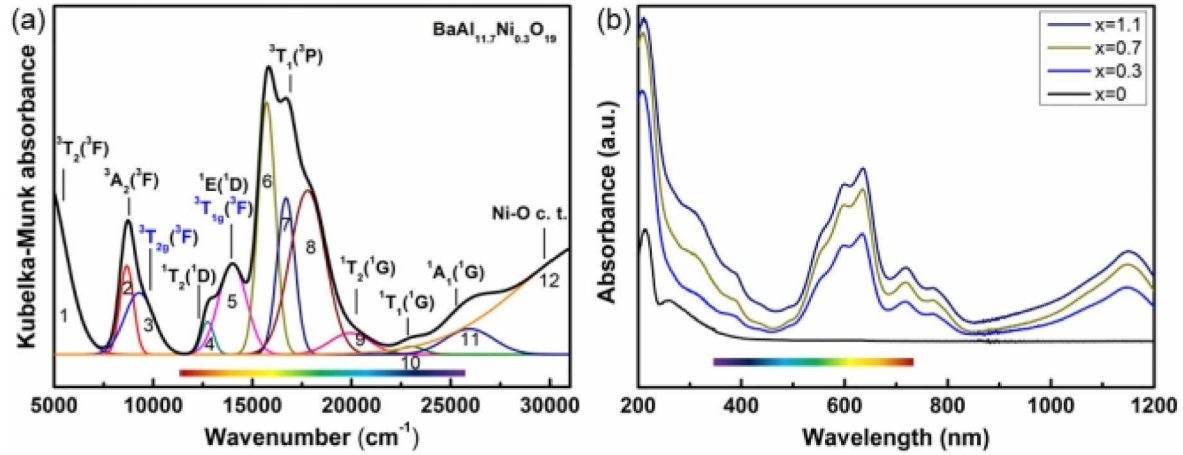

Fig. 29. (a) Fitting of Kubelka-Munk absorption spectrum of $BaAl_{11.7}Ni_{0.3}O_{19}$ bands; (b) The absorbance spectrum of $BaAl_{12-x}Ni_xO_{19}$ ($0 \leq x \leq 1.1$) [81].

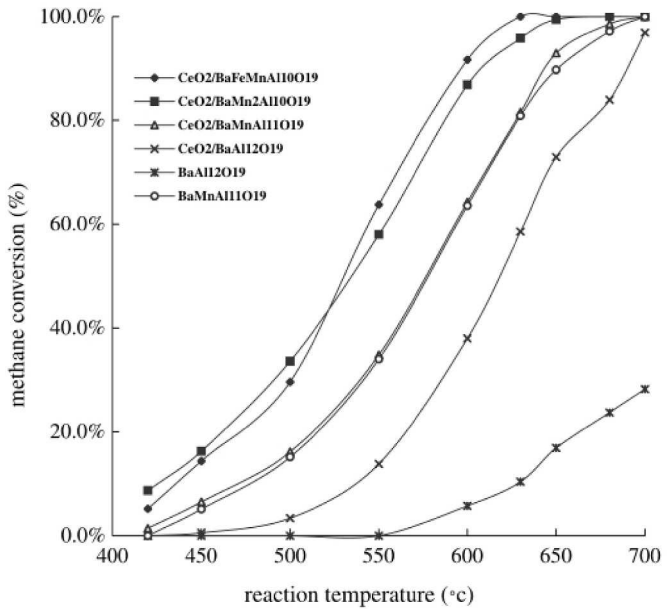

Fig. 30. Catalytic combustion of CH_4 over the catalysts [89].

Table 3
Catalytic activities expressed as $T_{10\%}$, $T_{50\%}$ and $T_{90\%}$ in °C [89].

Catalysts	$T_{10\%}$(°C)	$T_{50\%}$(°C)	$T_{90\%}$(°C)
$BaAl_{12}O_{19-\alpha}$	630	750	841
$BaMnAl_{11}O_{19-\alpha}$	470	580	655
$BaMn_2Al_{11}O_{19-\alpha}$	433	537	619
$CeO_2/BaAl_{12}O_{19-\alpha}$	535	618	690
$CeO_2/BaMnAl_{11}O_{19-\alpha}$	468	576	645
$CeO_2/BaMn_2Al_{10}O_{19-\alpha}$	426	534	611
$CeO_2/BaFeMnAl_{10}O_{19-\alpha}$	436	530	597

combustion. It is also applicable in the transesterification reaction of rapeseed oil with methanol under flow conditions [84] and steam reforming of tar [85].

Currently, methane has been used widely for industry, and methane combustion always involves nitrogen oxide (NO_x) production. Catalytic combustion with enhanced energy efficiency is a better way to reduce NO_x emissions. $BaAl_{12}O_{19}$ exhibits promising catalytic activity for methane combustion. To obtain better catalytic performance, different synthetic methods were attempted to increase its surface area. Teng et al. prepared nanoscale $BaAl_{12}O_{19}$ via a nonionic reverse microemulsion method and proved that needle-shaped $BaAl_{12}O_{19}$ is more conducive to methane combustion than spherical $BaAl_{12}O_{19}$ [86]. $BaMnAl_{11}O_{19-\alpha}$ was synthesized by supercritical drying (SCD) with alumina sol using a $(NH_4)_2CO_3$ coprecipitation precursor. By improving the surface area, the as-synthesized samples demonstrate high catalytic activity [87]. Yin et al. synthesized $BaAl_{12}O_{19}$ by the urea combustion method, which also improved the surface area [88]. To further improve the catalytic efficiency for methane combustion, Mn, Fe or multiple elements were doped into $BaAl_{12}O_{19}$, CeO_2–$BaAl_{12}O_{19}$ composite or both. As indicated in Fig. 30 and Table 3, Mn doping helped with the catalytic efficiency of $BaAl_{12}O_{19}$. $CeO_2/BaFeMnAl_{10}O_{19-\alpha}$ has the best performance as a combustion catalyst [87,89].

$BaAl_{12}O_{19}$ with proper reaction conditions can help to achieve almost complete conversion of rapeseed oil. The high thermal stability and high surface area make $BaAl_{12}O_{19}$ a catalyst for high-temperature reactions in steam reforming of tar. When Co metal particles are dispersed on $BaAl_{12}O_{19}$, $Co/BaAl_{12}O_{19}$ shows higher catalytic activity in the steam reforming of tar [85].

4.2. Catalytic properties of $BaAl_2O_4$

4.2.1. $BaAl_2O_4$ catalyzes the reaction of soot with NO_x

NO_x generated through petroleum combustion is known to be hazardous to the environment. $BaAl_2O_4$ exhibits potential in catalyzing the simultaneous removal of soot and NO_x. $BaAl_2O_4$ shows comparable catalytic efficiency to noble metal-based catalysts in NO_x trapping. However, the high cost and scarcity of noble metals make $BaAl_2O_4$ more promising. Compared with BaO, $BaAl_2O_4$ has a higher efficiency of NO_x reduction, as barium is engaged in a strong bond with aluminum to inhibit CO_2 adsorption [90,91]. Therefore, $BaAl_2O_4$ can be used as a new catalyst to replace noble metal-based catalysts.

NO_x is reduced to N_2 by carbon soot, and soot is oxidized to CO_2 in the process. The effect of $BaAl_2O_4$ is completely different under various O_2 partial pressures. In the absence of O_2, the reaction requires a higher temperature to make lattice oxygen atoms participate in the reaction. In the presence of O_2, the reaction mechanism is shown in Fig. 31. Nitrates and C(O) intermediates are the key precursors of the reaction. Initially, nitrite is formed by NO_x adsorption on the $BaAl_2O_4$ catalyst. With the presence of oxygen, the nitrites are readily oxidized into nitrates. The C(O) intermediates from carbon in the soot are preoxidized by NO, NO_2 and O_2. Finally, the redox of nitrate with these oxygenates releases CO_2, N_2 and a small quantity of N_2O, ultimately regenerating active sites on catalyst surfaces [92,93]. $BaAl_2O_4$ therefore realizes NO_x adsorption and

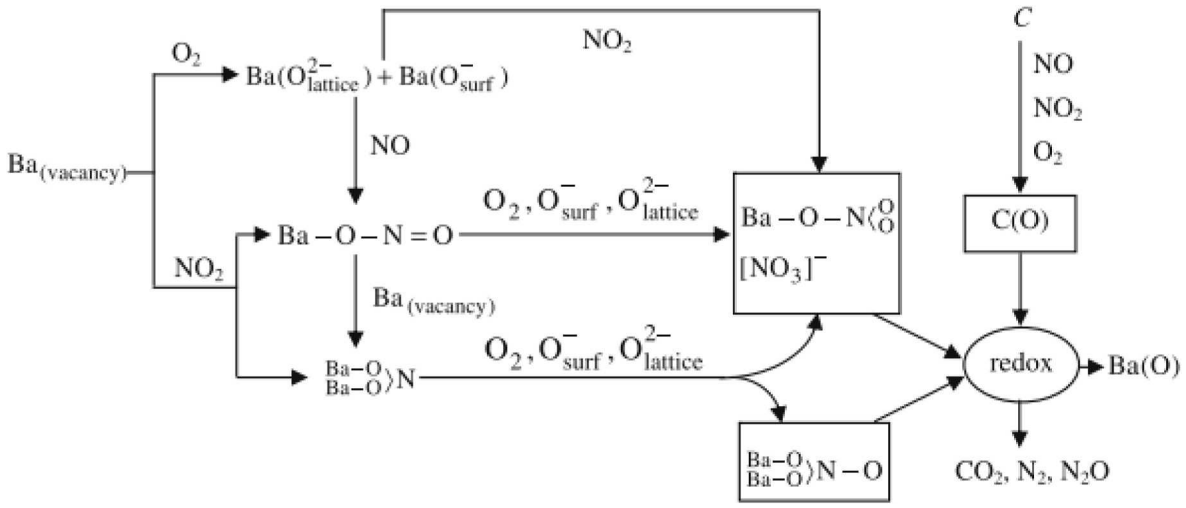

Fig. 31. Schematic mechanisms on the redox of soot and NO_x on $BaAl_2O_4$ surface [92].

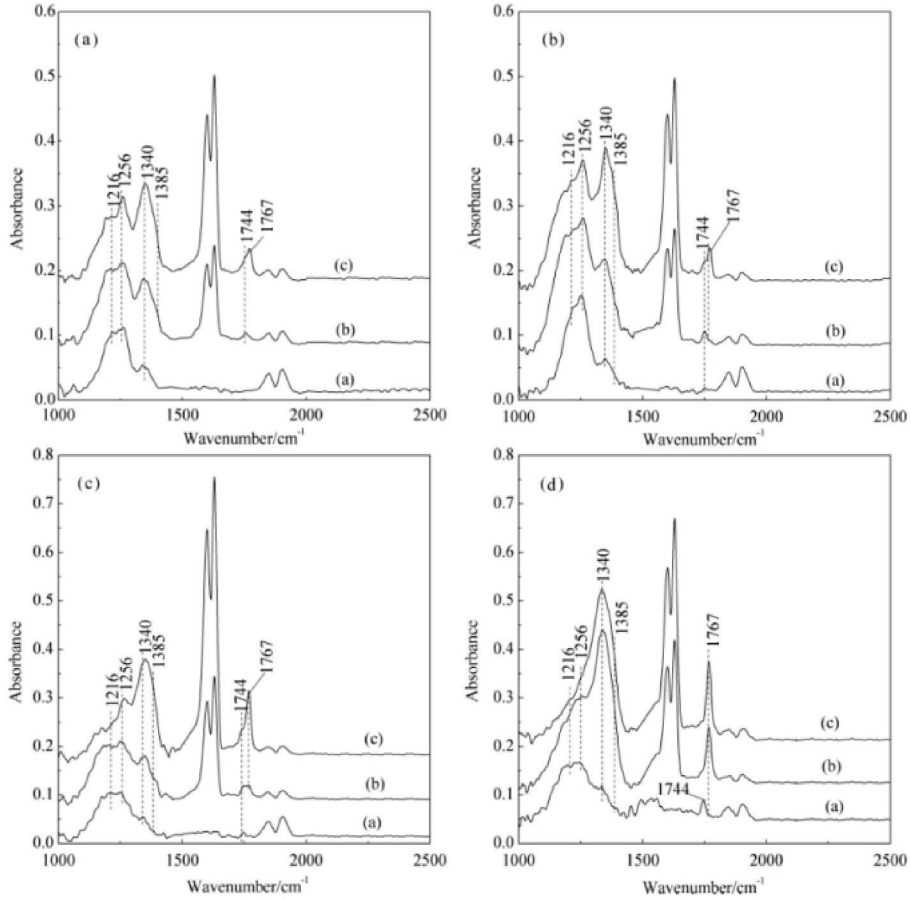

Fig. 32. The spectra were $BaAl_2O_4$ dwelling with gaseous reactants at (a) 150 °C, (b) 250 °C, (c) 350 °C and (d) 450 °C, the curves were gaseous reactants switched from (a) NO(0.5%)/He to (b) NO(0.5%)/O_2(2%)/He to (c) NO(0.5%)/O_2(5%)/He [94].

the reaction of soot with NO_x spontaneously.

Nitrates are easily produced on the catalyst surface in the presence of oxygen, so Li et al. studied the effect of oxygen concentration on the reaction of NO_x with soot. In Fig. 32, the bands at 1216 cm^{-1}, 1256 cm^{-1} and 1340 cm^{-1} are attributed to nitrites, and the bands at 1340 cm^{-1} 1385 cm^{-1} and 1744 cm^{-1} are attributed to nitrates. The intensities of the bands for nitrates further increase with increasing O_2 concentration. This is because more NO_2 is adsorbed, as well as the transformation of nitrites in the excess of O_2. As a consequence, the reaction of soot with NO_x is promoted, and the conversion efficiency of NO_x into N_2 and N_2O is improved. The intensities for the nitrates at 350 °C and 450 °C are obviously stronger than those at 150 °C and 250 °C. Therefore, high temperature also favors the formation of nitrates to promote the reaction of soot with NO_x [94]. In addition to oxygen concentration control, Yang et al. attempted to dope Mn at the Ba site to improve soot oxidation and NO_x reduction over a $BaAl_2O_4$ catalyst. A synergistic mechanism of manganese and barium is proposed to promote soot combustion. Among them, NO is captured by barium to form nitrite, and the generated nitrites are further transformed to nitrates facilitated by manganese, which finally oxidizes soot into CO_2 [95].

4.2.2. *$BaAl_2O_4$ photocatalysis*

$BaAl_2O_4$ with a strong light absorption capacity is also applied in photocatalysis. However, the high electron hole recombination rate, low charge transfer capacity and separation efficiency limit its applications. To solve this problem, doping noble metal ions or other active ions into $BaAl_2O_4$ is a good approach.

In photocatalysis, the key to $BaAl_2O_4$ catalysts are hydroxyl groups on the surface of the catalyst. After the $BaAl_2O_4$ catalyst absorbs

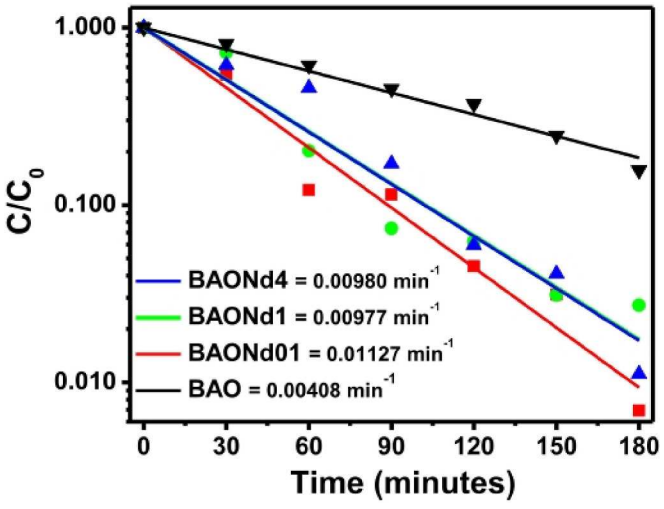

Fig. 33. Methylene blue photocatalytic degradation profiles under solar radiation [98].

photons, photogenerated electrons enter the conduction band of $BaAl_2O_4$ from the valence band. The electrons can be trapped by O_2 to form superoxide radicals (O_2^-). Additionally, corresponding positive holes are produced in the valence band that can produce highly reactive hydroxyl radicals. Hydroxyl radicals are powerful oxidizing reagents with an oxidation potential of 2.33 V and exhibits a high rate of reaction

with most organic and many inorganic solutes [96].

Zhu et al. doped Ag ions into $BaAl_2O_4$ to enhance the photocatalytic activity in toluene decomposition. After excitation by Ag, photogenerated electrons enter the conduction band of $BaAl_2O_4$, and some electrons will produce hydroxyl radicals [97]. Methylene blue is widely present in industrial wastewater and causes serious pollution and damage to the environment. To enhance the photocatalytic activity, Mumanga et al. doped Nd^{3+} into $BaAl_2O_4$. Then, they found that the catalyst had the best photocatalytic degradation rate with a 0.1 mol% Nd^{3+} doping percentage, as shown in Fig. 33 [98].

5. Conclusion

In the oxides currently reported in the $BaO–Al_2O_3$ system, with increasing Ba content, the stability of the compound decreases gradually. Therefore, $BaAl_{12}O_{19}$ and $BaAl_2O_4$ attract more research focus than other oxides. The structure and potential applications of $BaAl_{12}O_{19}$, $BaAl_2O_4$, $Ba_3Al_2O_6$, $Ba_4Al_2O_7$, and $Ba_7Al_2O_{10}$ are summarized. Although much work has been performed on the synthesis, structure analysis and property improvement of these oxides, there is still plenty of unknown knowledge on their detailed structure, photoluminescence property mechanism, potential applications and so on. With a better understanding of the oxides in the $BaO–Al_2O_3$ system, they will hopefully be able to be utilized in our daily life.

Acknowledgments

This work was supported by the National Natural Science Foundation of China under Grant No. 11230538, Youth Teacher International Exchange & Growth Program under the grant No. QNXM20220018. The work done at Oregon State University is supported by US National Science Foundation Grant No. DMR-2025615.

References

[1] Choudhary AK, Dwivedi A, Bahadur A, Rai SB. Enhanced upconversion from Er^{3+}/Yb^{3+} co-doped alkaline earth aluminates phosphor in presence Zn^{2+}: a comparative study. JLum 2019;210:135–41.
[2] Wei Y, Cao L, Lv L, Li G, Hao J, Gao J, Su C, Lin CC, Jang HS, Dang P, Lin J. Highly efficient blue emission and superior thermal stability of $BaAl_{12}O_{19}$:Eu^{2+} phosphors based on highly symmetric crystal structure. Chem Mater 2018;30:2389–99.
[3] Zhai B-g, Ma Q-l, Xiong R, Li X, Huang YM. Blue-green afterglow of $BaAl_2O_4$:Dy^{3+} phosphors. MaRBu 2016;75:1–6.
[4] Shannon RD, Prewitt CT. Effective ionic radii in oxides and fluorides. Acta Crystallogr Sect B Struct Crystallogr Cryst Chem 1969;25:925–46.
[5] Zhang R, Taskinen P. A phase equilibria study and thermodynamic assessment of the BaO-Al_2O_3 system. Calphad 2015;51:42–50.
[6] Groppi G, Assandri F, Bellotto M, Cristiani C, Forzatti P. The crystal structure of Ba-β-alumina materials for high-temperature catalytic combustion. JSSCh 1995;114:326–36.
[7] Hu J, Song E, Zhou Y, Zhang S, Ye S, Xia Z, Zhang Q. Non-stoichiometric defect-controlled reduction toward mixed-valence Mn-doped hexaaluminates and their optical applications. J Mater Chem C 2019;7:5716–23.
[8] Peng M, Qiu J, Yang l, Zhao C. Observation of Eu3+→Eu2+ in barium hexaaluminates with β′ or β-alumina structures prepared in air. OptMa 2004;27:591–5.
[9] Bellotto M, Artiolib G, Cristiani C, Forzattia P, Groppi G. On the crystal structure and cation valence of Mn in Mn-substituted Ba-β-Al2O3. JCat 1998;179:597–605.
[10] You H, Zhang J, Hong G, Zhang H. Luminescent properties of Mn^{2+} in hexagonal aluminates under ultraviolet and vacuum ultraviolet excitation. J Phys Chem C 2007;111:10657–61.
[11] Groppi G, Bellotto M, Cristiani C, Forzatti P, Villa P. Thermal evolution crystal structure and cation valence of Mn in substituted Ba-β-Al2O3 prepared via coprecipitation in aqueous medium. JMatS 1999;34:2609–20.
[12] Glasser FP, Glasser LSD. Crystal chemistry of some AB_2O_4 compounds. J Am Ceram Soc 1963;46:377–80.
[13] Huang S-Y, Mühll RVD, Ravez J, Chaminade JP, Hagenmuller P, Couzi M. A propos de la ferroeléctricité dans BaAl2O4. J Solid State Chem 1994;109:97–105.
[14] Sui-Yang H, Mühll RVD, Ravez J, Couzi M. Phase transition and symmetry in $BaAl_2O_4$. Fer 1994;159:127–32.
[15] Lazic B, Kahlenberg V, Kaindl R, Kremenović A. On the symmetry of $Ba_3Al_2O_6$ - X-ray diffraction and Raman spectroscopy studies. Solid State Sci 2009;11:77–84.
[16] Kahlenberg V. Crystal structure of $Ba_8[Al_3O_{10}][AlO_4]$, a novel mixed-anion Ba aluminate related to kilchoanite. MinM 2001;65:533–41.
[17] Priya GK, Padmaja P, Warrier KGK, Damodaran AD, Aruldhas G. Dehydroxylation and high temperature phase formation in sol-gel boehmite characterized by Fourier transform infrared spectroscopy. JMSL 1997;16:1584–7.
[18] Parida KM, Pradhan Amaresh C, Das J, Sahu N. Synthesis and characterization of nano-sized porous gamma-alumina by control precipitation method. MCP 2009;113:244–8.
[19] Lucio-Ortiz CJ, De la Rosa Javier Rivera, Ramirez Aracely Hernandez, Heredia JADlR, Angel Pd, Muñoz-Aguirre S, León-Covián LMD. Synthesis and characterization of Fe doped mesoporous Al_2O_3 by sol-gel method and its use in trichloroethylene combustion. JSGST 2011;58:374–84.
[20] Neuville DR, Cormier L, Massio D. Al coordination and speciation in calcium aluminosilicate glasses: effects of composition determined by 27Al MQ-MAS NMR and Raman spectroscopy. ChGeo 2006;229:173–85.
[21] Licheron M, Montouillout V, Millot F, Neuville DR. Raman and 27Al NMR structure investigations of aluminate glasses: $(1 - x)A_{12}O_3 - x$ MO, with M = Ca, Sr, Ba and $0.5 < x < 0.75$). J Non-Cryst Solids 2011:357.
[22] Coenen K, Gallucci F, Mezari B, Verhoeven T, Hensen E, Annaland MvS. Investigating the role of the different metals in hydrotalcite Mg/Al-based adsorbents and their interaction with acidic sorbate species. ChEnS 2019;200:138–46.
[23] Wang Y, Lei H, Jiang P, Liu L, Cui K, Cao W. Synthesis and optical properties of intense blue colors oxides based on Mn^{5+} in tetrahedral sites in $Ba_7Al_{2-x}Mn_xO_{10+y}$. Ceram Int 2021;47:686–91.
[24] Liao S, Ji X, Liu Y, Zhang J. Highly efficient and thermally stable blue-green (Ba0.8Eu0.2O)(Al2O3)4.575x(1+x) phosphor through structural modification. ACS Appl Mater Interfaces 2018;10:39064–73.
[25] Guo Y, Zhou S, Sun X, Lao X, Yuan H. $BaAl_{12}O_{19}$:Eu^{2+} phosphors: molten salt flux synthesis and blue emission with high color purity and excellently thermal stability. JLum 2019;211:271–5.
[26] Singh V, Chakradhar RPS, Rao JL, Ko I, Kwak H-Y. Luminescence and EPR studies of Eu^{2+} doped $BaAl_{12}O_{19}$ blue light emitting phosphors. JLum 2010;130:703–8.
[27] Xiao L, He M, Tian Y, Chen Y, Karaki T, Li W, Xie Y, Zhang L. Study on luminescence properties of Eu^{2+} in $BaAl_{12}O_{19}$ matrix. J Nanosci Nanotechnol 2010;10:2131–4.
[28] Wang Z, Liu Y, Chen J, Fang M, Huang Z, Mei L. Color tunable $Ba_{0.79}Al_{10.9}O_{17.14}$:*x*Eu phosphor prepared in air via valence state control. J Adv Ceram 2017;6:81–9.
[29] Xiao L, He M, Tian Y, Chen Y, Karaki T, Zhang L, Wang N. Structure and luminescence properties of new green-emitting phosphor $BaAl_{12}O_{19}$:Tb. JaJAP 2007;46:5871–3.
[30] Jeon HS, Kim SK, Park HL, Kim GC, Bang JH, Lee M. Observation of two independent energy transfer mechanisms in $BaAl_{12}O_{19}$: $Ce^{3+}_{0.06}$+Eu^{2+}_x phosphor. SSCom 2001;120:221–5.
[31] Xiao L, Xie Y, He M, Chen Y, Li W, Yu W. Luminescence properties of $BaAl_{12}O_{19}$:Tb, Ce and energy transfer between Ce^{3+}, Tb^{3+}. J Rare Earths 2010;28:225–8.
[32] Xie Y, Xiao LJ, He MR, Chen YJ, Li WZ, Yu WK. Study on luminescence behavior of $BaAl_{12}O_{19}$:Tb, Eu. J Nanosci Nanotechnol 2011;11:9908–11.
[33] Xiao LJ, Xie Y, He MR, Chen YJ, Geng XJ, Li WZ. Luminescent properties of $BaAl_{12}O_{19}$:Tb, Dy phosphors prepared by sol-gel method. J Nanosci Nanotechnol 2014;14:4570–3.
[34] Singh V, Chakradhar RPS, Rao JL, Kwak H-Y. Investigations on green-emitting, Mn^{2+}: $BaAl_{12}O_{19}$ phosphors obtained by solution combustion process. JMatS 2011;46:3928–34.
[35] Jun Z, Yu-Hua W, Bi-Tao L, Ji-Di L. Morphology and photoluminescence of $BaAl_{12}O_{19}$:Mn^{2+} green phosphor prepared by flux method. Chin Phys B 2010;19:127809.
[36] Yadav RS, Pandey SK, Pandey AC. $BaAl_{12}O_{19}$:Mn^{2+} green emitting nanophosphor for PDP application synthesized by solution combustion method and its Vacuum Ultra-Violet Photoluminescence Characteristics. JLum 2011;131:1998–2003.
[37] Dong QZ, He L, Li WS, Sun WM. The fabrication of one-dimensional $BaAl_{12}O_{19}$:Mn^{2+} phosphors by electrospinning method. MSF 2016;852:565–72.
[38] Wang Y, Xu X, Yin L, Hao L. High photoluminescence of Si-N-Co-doped $BaAl_{12}O_{19}$:Mn^{2+} green phosphors. Electrochem Solid State Lett 2010;13:J119–21.
[39] Liu B, Wang Y, Wen Y, Zhang F, Zhu G, Zhang J. Photoluminescence properties of S-doped $BaAl_{12}O_{19}$:Mn^{2+} phosphors for plasma display panels. MatL 2012;75:137–9.
[40] Wang YH, Li F. Synthesis of $BaAl_{12}O_{19}$:Mn^{2+} nanophosphors by a reverse microemulsion method and its photoluminescence properties under VUV excitation. JLum 2007;122–123:866–8.
[41] Zhou J, Wang Y, Liu B, Lu Y. Effect of H_3BO_3 on structure and photoluminescence of $BaAl_{12}O_{19}$:Mn^{2+} phosphor under VUV excitation. JAllC 2009;484:439–43.
[42] Singh V, Sivaramaiah G, Rao JL, Sripada S, Kim SH. An electron paramagnetic resonance and optical study of Cr doped $BaAl_{12}O_{19}$ powders. Ceram Int 2014;40:9629–36.
[43] Zhong R, Zhang J. Red photoluminescence due to energy transfer from Eu^{2+} to Cr^{3+} in $BaAl_{12}O_{19}$. JLum 2010;130:206–10.
[44] Singh V, Sivaramaiah G, Rao JL, Kim SH. Optical and EPR properties of $BaAl_{12}O_{19}$:Eu^{2+}, Mn^{2+} phosphor prepared by facile solution combustion approach. JLum 2015;157:74–81.
[45] Zhu Y, Li C, Deng D, Chen B, Yu H, Li H, Wang L, Shen C, Jing X, Xu S. A high-sensitivity dual-mode optical thermometry based on one-step synthesis of Mn2+:BaAl12O19-Mn4+:SrAl12O19 solid solution phosphors. JAllC 2021:853.
[46] Zhu Y, Li C, Deng D, Yu H, Li H, Wang L, Shen C, Jing X, Xu S. High-sensitivity based on Eu^{2+}/Cr^{3+} co-doped $BaAl_{12}O_{19}$ phosphors for dual-mode optical thermometry. JLum 2021;237.

[47] Oliveira NA, Bispo Jr AG, Lima SAM, Pires AM. Red-emitting $BaAl_2O_4$:Eu^{3+} synthesized via Pechini and sol-gel routes: a comparison of luminescence and structure. JMatS 2022;57:170–84.

[48] Peng M, Hong G. Reduction from Eu^{3+} to Eu^{2+} in $BaAl_2O_4$:Eu phosphor prepared in an oxidizing atmosphere and luminescent properties of $BaAl_2O_4$:Eu. JLum 2007; 127:735–40.

[49] Nakauchi D, Okada G, Kato T, Kawaguchi N, Yanagida T. Crystal growth and scintillation properties of Eu:$BaAl_2O_4$ crystals. Radiat Measur 2020;135.

[50] He Q, Qiu G, Xu X, Qiu J, Yu X. Photostimulated luminescence properties of Eu^{2+}-doped barium aluminate phosphor. Luminescence 2015;30:235–9.

[51] Aitasalo T, Hölsä J, Jungner H, Lastusaari M, Niittykoski J. Thermoluminescence study of persistent luminescence materials: Eu^{2+}- and R^{3+}-doped calcium aluminates, $CaAl_2O_4$:Eu^{2+},R^{3+}. J Phys Chem B 2006;110:4589–98.

[52] Dorenbos P. Mechanism of persistent luminescence in Eu2+ and Dy3+ codoped aluminate and silicate compounds. JElS 2005:152.

[53] Clabau F, Rocquefelte X, Jobic S, Deniard P, Whangbo M-H, Garcia A, Mercier TL. Mechanism of phosphorescence appropriate for the long-lasting phosphors Eu^{2+}-doped $SrAl_2O_4$ with codopants Dy^{3+} and B^{3+}. Chem Mater 2005;17:3904–12.

[54] Lephoto MA, Ntwaeaborwa OM, Pitale SS, Swart HC, Botha JR, Mothudi BM. Synthesis and characterization of $BaAl_2O_4$:Eu^{2+} co-doped with different rare earth ions. Phys B Condens Matter 2012;407:1603–6.

[55] Rodrigues LCV, Hölsä J, Carvalho JM, Pedroso CCS, Lastusaari M, Felinto MCFC, Watanabe S, Brito HF. Co-dopant influence on the persistent luminescence of $BaAl_2O_4$:Eu^{2+},R^{3+}. Phys B Condens Matter 2014;439:67–71.

[56] Cheng B, Fang L, Zhang Z, Xiao Y, Lei S. $BaAl_2O_4$:Eu^{2+}, Dy^{3+} nanotube synthesis by heating conversion of homogeneous coprecipitates and afterglow characteristics. J Phys Chem C 2011;115:1708–13.

[57] Zhang J, Xiao Q, Liu Y. Synthesis and characterization of needle-like $BaAl_2O_4$:Eu, Dy phosphor via. J Rare Earths 2013;31:342–6.

[58] Sun F, Zhao J. Blue-green $BaAl_2O_4$:Eu^{2+},Dy^{3+} phosphors synthesized via combustion synthesis method assisted by microwave irradiation. J Rare Earths 2011;29:326–9.

[59] Ianoş R, Lazău R, Boruntea RC. Solution combustion synthesis of bluish-green $BaAl_2O_4$: Eu^{2+}, Dy^{3+} phosphors. Ceram Int 2015;41:3186–90.

[60] Bartwal KS, Ryu H. Long persistence in Sr/$BaAl_2O_4$: Eu^{2+}: Dy^{3+} green phosphor. Resour Process 2008;55:120–3.

[61] Ryu H, Singh BK, Bartwal KS. Effect of Sr substitution on photoluminescent properties of $BaAl_2O_4$:Eu^{2+}, Dy^{3+}. Phys B Condens Matter 2008;403:126–30.

[62] Silva DC, Lima AS, Silva JHL, Rezende MVS, Sampaio DV, Ballato J, Silva RS. Laser sintering and influence of the Dy concentration on $BaAl_2O_4$:Eu^{2+}, Dy^{3+} persistent luminescence ceramics. J Eur Ceram Soc 2021;41:3629–34.

[63] Roh H-S, Cho I-S, An J-S, Cho CM, Noh TH, Yim DK, Kim D-W, Hong KS. Enhanced photoluminescence property of Dy^{3+} co-doped $BaAl_2O_4$:Eu^{2+} green phosphors. Ceram Int 2012;38:443–7.

[64] Ma J, Fan D, Niu B, Lan X. Enhanced afterglow property of $BaAl_2O_4$:Eu^{2+}, Dy^{3+} phosphors by adding Li_2CO_3. Function Mater Lett 2016;10.

[65] Chatterjee R, Das GC, Chattopadhyay KK. Synthesis and characterization of highly luminescent green emitting $BaAl_2O_4$:Tb^{3+} nanophosphors. Mater Today Proc 2019; 18:1132–7.

[66] Chatterjee R, Saha S, Panigrahi K, Ghorai UK, Das GC, Chattopadhyay KK. Blue emitting $BaAl_2O_4$:Ce^{3+} nanophosphors with high color purity and brightness for white LEDs. Microsc Microanal 2019;25:1466–70.

[67] Suriyamurthy N, Panigrahi BS. Luminescence of $BaAl_2O_4$:Mn^{2+}, Ce^{3+} phosphor. JLum 2007;127:483–8.

[68] Singh V, Natarajan V, Kim D-K. Combustion synthesis and luminescence properties of $MgSrAl_{10}O_{17}$:$Mn^{2+}$and $BaAl_2O_4$:Mn^{4+}. REDS 2008;163:199–206.

[69] Maphiri VM, Mhlongo MR, Hlatshwayo TT, Motaung TE, Koao LF, Motloung SV. Citrate sol-gel synthesis of BaAl2O4:x% Cu2+ ($0 \leq x \leq 1$) nano-phosphors: structural, morphological and photoluminescence properties. OptMa 2020;109.

[70] Melo SS, Andrade AB, Bispo GFC, Carvalho JC, Macedo ZS, Valerio MEG. X-ray absorption spectroscopy and tunable color emission study of the Mn-co-doped $BaAl_2O_4$: Ce phosphor under synchrotron radiation. OptMa 2019;91:401–7.

[71] Ryu H, Bartwal KS. Investigations on luminescence characteristics of Eu and Cr codoped $BaAl_2O_4$. MCP 2008;111:186–9.

[72] Ryu H, Bartwal KS. Effect of Ti co-doping on photoluminescence characteristics of Eu:$BaAl_2O_4$. JAllC 2013;574:331–4.

[73] You W, Xiao Z, Lai F, Ye X, Zhang Q, Jiang H, Wang C, Liao J, Liu X, Zhong S. Synthesis and photoluminescence properties of $Ba_3Al_2O_6$:Eu^{3+} red phosphor. JMatS 2016;51:5403–11.

[74] Yerpude AN, Dhoble SJ. Luminescent properties of $Eu^{2+}$and Dy^{3+} ions in $Ba_4Al_2O_7$ phosphor for solid state lighting. JLum 2012;132:1781–5.

[75] Zhou Y, Jiang P, Lei H, Li Y, Cao W, Kuang J. Synthesis and properties of novel turquoise-green pigments based on $BaAl_{2-x}Mn_xO_{4+y}$. Dyes Pigments 2018;155: 212–7.

[76] Wang Y, Lei H, Jiang P, Cui K, Liu L, Li B, Cao W. Synthesis and optical properties of Mn-doped $Ba_3Al_2O_6$ intense blue oxides. OptMa 2020;109.

[77] Jiang P, Xiao T, Zhou Y, Kuang J, Wang Q, Cao W. Facile synthesis of brownmillerite-type oxides $Ba_2In_{2-x}Mn_xO_{5+x}$ through a microwave-assisted process. Solid State Sci 2017;65:1–5.

[78] Kim SW, Sim GE, Ock JY, Son JH, Hasegawa T, Toda K, Bae DS. Discovery of novel inorganic Mn^{5+}-doped sky-blue pigments based on $Ca_6BaP_4O_{17}$: crystal structure, optical and color properties, and color durability. Dyes Pigments 2017;139:344–8.

[79] Gomes MA, Andrade AB, Rezende MVdS, Valerio MEG. Production of Eu-doped $BaAl_2O_4$ at low temperature via an alternative sol-gel method using PVA as complexing agent. JPCS 2017;102:74–8.

[80] Gedekar KA, Wankhede SP, Moharil SV, Belekar RM. d-f luminescence of Ce^{3+} and Eu^{2+} ions in $BaAl_2O_4$, $SrAl_2O_4$ and $CaAl_2O_4$ phosphors. J Adv Ceram 2017;6: 341–50.

[81] Wang Y, Cheng Q, Jiang P, Liu L, Cui K, Li Y. Synthesis and properties of novel blue zirconia ceramic based on Co/Ni-doped $BaAl_{12}O_{19}$ blue chromophore. J Eur Ceram Soc 2022;42:543–51.

[82] Costa G, Ribeiro MJ, Hajjaji W, Seabra MP, Labrincha JA, Dondi M, Cruciani G. Ni-doped hibonite ($CaAl_{12}O_{19}$): a new turquoise blue ceramic pigment. J Eur Ceram Soc 2009;29:2671–8.

[83] Ardit M, Borcănescu S, Cruciani G, Dondi M, Lazău I, Păcurariu C, Zanelli C, McKittrick J. Ni-Ti codoped hibonite ceramic pigments by combustion synthesis: crystal structure and optical properties. J Am Ceram Soc 2016;99:1749–60.

[84] Ivanova AS, Sherstyuk OV, Bukhtiyarova MV, Kukushkin RG, Matvienko LG, Plyasova LM, Kaichev VV, Simonov AN, Yakovlev VA. Performance of Ba-containing catalysts in the transesterification reaction of rapeseed oil with methanol under flow conditions. Catal Commun 2012;18:156–60.

[85] Li D, Ishikawa C, Koike M, Wang L, Nakagawa Y, Tomishige K. Production of renewable hydrogen by steam reforming of tar from biomass pyrolysis over supported Co catalysts. IJHE 2013;38:3572–81.

[86] Teng F, Tian Z, Xu J, Xiong G, Lin L. Synthesis of nano-sized $BaAl_{12}O_{19}$ via nonionic reverse microemulsion method: I. Effect of the microemulsion structure on the paticle morphology. Stud Surf Sci Catal 2004;147:493–8.

[87] Li S, Liu H, Zhao X, Wang X. A cost-effective preparation method of Ba-hexaaluminate nanoparticles for catalytic combustion of methane. MatL 2007;61: 3935–8.

[88] Yin F, Ji S, Wu P, Zhao F, Li C. Preparation, characterization, and methane total oxidation of $AAl_{12}O_{19}$ and $AMAl_{11}O_{19}$ hexaaluminate catalysts prepared with urea combustion method. J Mol Catal Chem 2008;294:27–36.

[89] Li S, Wang X. The Ba-hexaaluminate doped with CeO_2 nanoparticles for catalytic combustion of methane. Catal Commun 2007;8:410–5.

[90] Hodjati S, Bernhardt P, Petit C, Pitchon V, Kiennemann A. Removal of NO_x: Part I. Sorption/desorption processes on barium aluminate. Appl Catal B Environ 1998; 19:209–19.

[91] Hodjati S, Bernhardt P, Petit C, Pitchon V, Kiennemann A. Removal of NO_x: Part II. Species formed during the sorption/desorption processes on barium aluminates. Appl Catal B Environ 1988;19:221–32.

[92] Lin H, Li Y, Shangguan W, Huang Z. Soot oxidation and NO_x reduction over $BaAl_2O_4$ catalyst. CoFl 2009;156:2063–70.

[93] Li YJ, Lin H, Shangguan WF, Huang Z. Properties of $BaAl_2O_4$ in the simultaneous removal of soot and NO_x. Chem Eng Technol 2007;30:1426–33.

[94] Li YJ, Lin H, Shangguan WF, Huang Z. The effect of oxygen concentration on the reaction of NO_x with soot over $BaAl_2O_4$. Chem Eng Technol 2008;31:138–42.

[95] Yang G, Li Y, Men Y. Synergistic catalysis effect of Mn-promoted $BaAl_2O_4$ catalysts on catalytic performance for soot combustion. Catal Commun 2015;69:202–6.

[96] Gogate PR, Pandit AB. A review of imperative technologies for wastewater treatment I: oxidation technologies at ambient conditions. Adv Environ Res 2004; 8:501–51.

[97] Zhu Z, Liu F, Zhang W. Fabricate and characterization of Ag/$BaAl_2O_4$ and its photocatalytic performance towards oxidation of gaseous toluene studied by FTIR spectroscopy. MaRBu 2015;64:68–75.

[98] Mumanga TJ, Díaz-Torres LA, Gómez-Solís C. Nd3+ doped BaAl2O4 for enhanced photocatalytic degradation of methylene blue. MatL 2021:292.